Quantifying the Uncertainty of the Future Hydrological Impacts of Climate Change: Comparative Analysis of an Advanced Hierarchical Sensitivity in Humid and Semiarid Basins

JIALI JU,[a,h] HENG DAI,[b,c,h] CHUANHAO WU,[d] BILL X. HU,[a,d] MING YE,[e] XINGYUAN CHEN,[f] DONGWEI GUI,[g] HAIFAN LIU,[a] AND JIN ZHANG[d]

[a] *School of Water Resources and Environment, China University of Geosciences, Beijing, China*
[b] *State Key Laboratory of Biogeology and Environmental Geology, China University of Geosciences, Wuhan, China*
[c] *State Key Laboratory of Desert and Oasis Ecology, Xinjiang Institute of Ecology and Geography, Chinese Academy of Sciences, Urumqi, China*
[d] *Institute of Groundwater and Earth Sciences, Jinan University, Guangzhou, China*
[e] *Department of Earth, Ocean, and Atmospheric Science, Florida State University, Tallahassee, Florida*
[f] *Pacific Northwest National Laboratory, Richland, Washington*
[g] *Cele National Station of Observation and Research for Desert–Grassland Ecosystem, Xinjiang Institute of Ecology and Geography, Chinese Academy of Sciences, Urumqi, China*

(Manuscript received 30 January 2020, in final form 22 December 2020)

ABSTRACT: Comparison and quantification of different uncertainties of future climate change involved in the modeling of a hydrological system are highly important for both hydrological modelers and policy-makers. However, few studies have accurately estimated the relative importance of different sources of uncertainty at different spatiotemporal scales. Here, a hierarchical sensitivity analysis framework (HSAF) incorporated with a variance-based global sensitivity analysis is developed to quantify the spatiotemporal contributions of different uncertainties in hydrological impacts of climate change in two different climatic (humid and semiarid) basins in China. The uncertainty sources include three emission scenarios (ESs), 20 global climate models (GCs), three hydrological models (HMs), and the associated sensitive hydrological parameters (PAs) screened and sampled by the Morris and Latin hypercube sampling methods, respectively. The results indicate that the overall trend of uncertainty is PA > HM > GC > ES, but their uncertainties have discrepancies in projections of different hydrological variables. The HM uncertainty in annual and monthly discharge projections is generally larger than the PA uncertainty in the humid basin than semiarid basin. The PA has greater uncertainty in extreme hydrological event (annual peak discharge) projections than in annual discharge projections for both basins (particularly for the humid basin), but contributes larger uncertainty to annual and monthly discharge projections in the semiarid basin than humid basin. The GC contributes larger uncertainty in all the hydrological variables projections in the humid basin than semiarid basin, while the ES uncertainty is rather limited in both basins. Overall, our results suggest there is greater spatiotemporal variability of hydrological uncertainty in more arid regions.

KEYWORDS: Climate change; Hydrology; Uncertainty; Sensitivity studies

1. Introduction

It is widely accepted that the most certain impact of future climate change is an increase in temperature throughout the world, particularly in the Northern Hemisphere (IPCC 2007, 2013). Global warming is expected to intensify the hydrological cycle and alter evapotranspiration with consequences for water resources (Abbaspour et al. 2009; Arnell 1999, 2004; Piao et al. 2010; Thompson et al. 2013; Vörösmarty et al. 2000), ecosystem services (Hoegh-Guldberg and Bruno 2010; Matthews and Quesne 2009; Preston 2002), and feedback to regional and global climates (Jung et al. 2010). Assessments of the hydrologic impacts of future climate change over large domains are commonly performed by coupling atmospheric climate projections from global climate models (GCs) and regional climate models with land surface schemes and hydrological models (e.g., Alfieri et al. 2015; Chen et al. 2011a,b, 2017; Raje and Mujumdar 2010; Gädeke et al. 2014; Habets et al. 2013; Jha and Gassman 2014; Kay et al. 2009; Lu et al. 2018; Maurer and Duffy 2005; Stephens et al. 2018; Wu et al. 2014, 2015; Xu et al. 2013; Zhang et al. 2011).

Uncertainty is inevitable and important in numerical models, especially complex hydrological models of future climate change impacts (Kay et al. 2009; Neuman 2003; Refsgaard et al. 2007). Uncertainties arise from variant sources, including unpredictable future conditions, lack of knowledge or data for systems, and variability in natural characteristics (Neuman 2003; Refsgaard et al. 2007; Rubin et al. 2010; Tartakovsky 2013). To determine the future impacts of climate change, the GC and greenhouse gas emission scenarios (ESs) are generally considered to be the two major uncertain factors influencing the assessment of hydrologic systems (Chen et al. 2011a,b; Kay et al. 2009; Liu et al. 2013; Minville et al. 2008; Thompson et al. 2013; Wilby and Harris 2006; Wu et al. 2015; Xu et al. 2013).

In addition to the uncertainty in the GC and ES, other sources of uncertainty, such as hydrological model (HM)

Supplemental information related to this paper is available at the Journals Online website: https://doi.org/10.1175/JHM-D-20-0016.s1.

[h] These authors contributed equally to this work.

Corresponding author: Chuanhao Wu, wuch0907@jnu.edu.cn

DOI: 10.1175/JHM-D-20-0016.1

uncertainty and hydrological parametric (PA) uncertainty, have also been found to be important for hydrological impact assessments. For example, Chen et al. (2011b, 2013) and Teutschbein et al. (2011) noted that the dynamic and statistical approaches for quantifying the impacts of climate change on hydrological systems are considerably influenced by uncertainty. Wilby (2005) investigated the impact of climate change on the monthly flow of the Thames River by considering the effect of PAs and showed that PA uncertainty is comparable in size to ES uncertainty. Jiang et al. (2007) investigated the hydrological impacts of climate change in the Dongjiang basin in southern China by comparing six HMs, and the results emphasized a large difference in modeling hydrological variables (e.g., runoff, evapotranspiration, and soil moisture). This finding has been confirmed by Najafi et al. (2011), who suggested that HM selection is necessary before assessing hydrologic climate change impacts.

Estimation of the importance of different uncertainty sources in climate and hydrological model systems is essential for modelers and managers, and sensitivity analysis (SA) is required for this estimation process. From the uncertainty viewpoint, SA focuses on quantifying the uncertainty from different uncertain model inputs that contribute to the model predictions (Dai and Ye 2015; Saltelli et al. 2010). In general, SA can generally be classified into local [e.g., one-at-a-time (OAT)] and global methods (Song et al. 2013; Dai and Ye 2015). The main shortcoming of local SA is computing the local response of the model output for a certain parameter in a narrow range of parameters (Saltelli 2000; Song et al. 2015; Valkó et al. 2018; Yang 2011). Compared with local SA, global SA considers the impact over the entire parameter space (Bennett et al. 2018; Bianchi Janetti et al. 2019; van Griensven et al. 2006) and therefore has been widely used in two broad categories: qualitative (e.g., the Morris method and multiple regression method) and quantitative (e.g., metamodel-based, variance-based, moment-independent-based, and information-entropy-based) methods (Khorashadi Zadeh et al. 2017; Morris 1991; Sobol' 1993; Song et al. 2013, 2015; Zeng et al. 2012). Recently, numerous studies have investigated the uncertainty of climatic and hydrological models using global SA methods (Chen et al. 2011b, 2013; Dobler et al. 2012; Nóbrega et al. 2011; Bastola et al. 2011; Shen et al. 2018; Teng et al. 2012).

Among the numerous global SA methods, variance-based SA is widely used in climatic and hydrological models because of its advantages of model independence and capability of providing mathematically rigorous and accurate measurements of the importance of different model uncertainty sources (Aryal et al. 2019; Bosshard et al. 2013; Chu-Agor et al. 2011; Saltelli 2000; Song et al. 2015; Vetter et al. 2017). However, there are two challenges in applying conventional variance-based global SA in climatic and hydrological models. The first challenge is the huge computational cost, and the second challenge is the complex relationship among the variant uncertainty sources. Conventional variance-based SA ignores the dependence or deterministic relationships of different uncertainty sources and fails to consider combinations of uncertain model inputs based on their characteristics (Dai et al. 2019; Bennett et al. 2018; Hattermann et al. 2018; Su et al. 2017). For example, GC uncertainty is caused by different atmospheric, oceanic and land processes in different GCs. GCs are used to simulate meteorological variables (e.g., precipitation and temperature) according to ESs. The ES and GC jointly play the role of forcing inputs in HMs. HM uncertainty is caused by different conceptual or mathematical formulations, and each HM has a distinct set of PAs that are subject to PA uncertainty. Therefore, PA uncertainty depends on HM, ES, and GC uncertainties; HM uncertainty depends on ES and GC uncertainties; and GC uncertainty depends on ES uncertainty.

Recently, Dai et al. (2017a,b) developed a hierarchical SA methodology that integrates the variance-based SA method with the hierarchical uncertainty framework. The hierarchical sensitivity analysis framework (HSAF) is capable of grouping different model uncertainty sources and considering the dependence relationships among these uncertain inputs, and has been suggested to provide useful and solid information for modelers about the importance of uncertain model inputs (Dai et al. 2017a). In this study, for the first time, the HSAF has been improved and modified to be suitable for a hydrologic climate model system by considering four sources of uncertainty (ES, GC, HM, and PA) on the basis of Dai et al. (2017a,b). Particularly, to reduce the workload of parameter calibration and validation as well as the computational cost, the Morris method is used to screen the most sensitive PAs of HMs, and the Latin hypercube sampling (LHS) method is used to estimate the sensitivity indices from sensitive PAs.

By extending the HSAF, this study conducts a comprehensive and quantitative SA of climate-influenced hydrological modeling in two different climatic basins [Beijiang River basin (BRB) and Liao River basin (LRB)] using continuous simulations of river flows. Two different HSAFs are implemented to explore the spatiotemporal variability of uncertainty: the four-layer HSAF considering four uncertainty sources (ES, GC, HM, and PA) for river discharge projections at the intra-annual and the interannual scale and the three-layer HSAF considering three uncertainty sources (ES, GC, and PA) for surface runoff depth projections at the grid scale. By providing a pilot example of uncertainty quantization in climate-influenced hydrological models, we aim to 1) identify the relative contribution of each uncertainty source to the model outputs and 2) test the spatiotemporal variations of general sources of uncertainty in hydrological predictions in the context of climate change. The HSAF used in this study is mathematically rigorous and general and can be applied to a wide range of hydrologic and environmental models that consider climate change, which improves our understanding of how climate influences the hydrological system.

2. Methodology

a. Sensitivity indices for the HSAF

The core of the variance-based HSAF is the variance decomposition of model outputs (Saltelli et al. 1998, 1999, 2010; Saltelli and Sobol' 1995). For a model with the form of

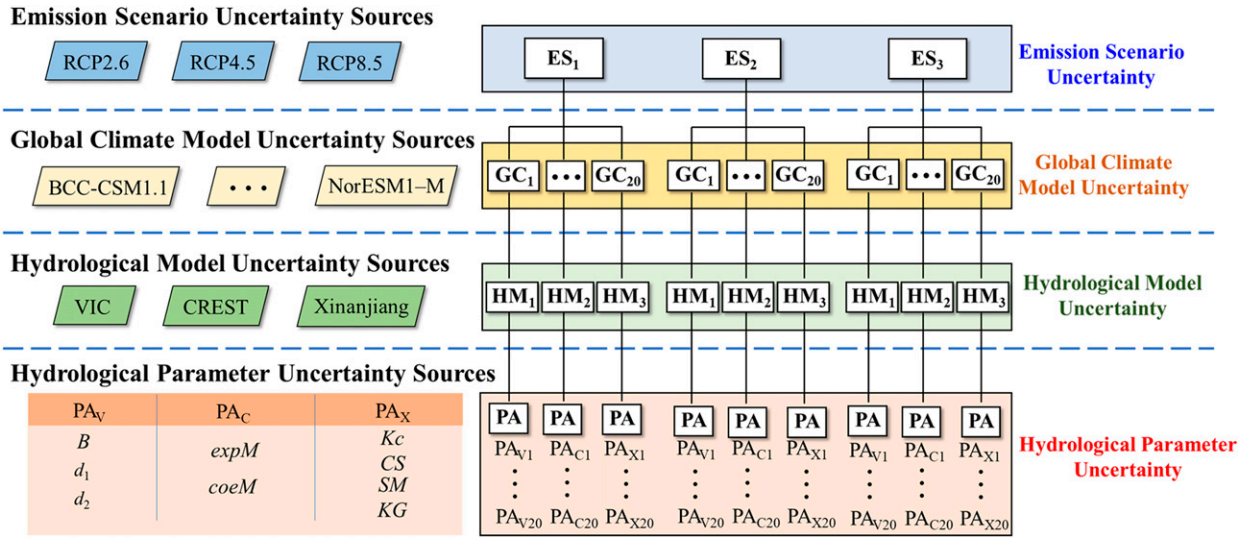

FIG. 1. Four-layer HSAF with the GC, ES, HM, and PA. **ES**, **GC**, **HM**, and **PA** represent the set of multiple greenhouse gas emission scenarios, multiple global climate models, multiple hydrological models, and the parameters for a given model, respectively. By neglecting HM uncertainty, this HSAF can be reduced to the three-layer HSAF, which considers only **ES**, **GC**, and **PA**.

$\Delta = f(\boldsymbol{\theta}) = f(\theta_1, \ldots, \theta_k)$, where Δ is the model output and $\boldsymbol{\theta} = \{\theta_1, \ldots, \theta_k\}$ is a set of uncertain model inputs, the total variance can be decomposed as

$$V(\Delta) = V_{\theta_i}[E_{\theta_{\sim i}}(\Delta|\theta_i)] + E_{\theta_i}[V_{\theta_{\sim i}}(\Delta|\theta_i)], \tag{1}$$

In this equation, the first term on the right-hand side is the partial variance contributed by θ_i and the second term represents the partial variance caused by the model inputs except θ_i. The first-order sensitivity index is thus defined as $S_i = V_{\theta_i}[E_{\theta_{\sim i}}(\Delta|\theta_i)]/V(\Delta)$. This index measures the percentage of output uncertainty contributed by θ_i and estimates its relative importance compared to other uncertain inputs.

This variance decomposition technique has been recursively applied by Dai and Ye (2015) and Dai et al. (2017a) to a three-layer HSAF in a complex groundwater reactive transport model. Based on Dai et al. (2017a), we developed the four-layer HSAF, which considers uncertainties from the ES, GC, HM, and PA [section 2a(1)], and the three-layer HSAF, which considers uncertainties from the ES, GC, and PA [section 2a(2)], for the hydrologic climate model system.

1) FOUR-LAYER HSAF

As shown in Fig. 1, the total variance in the model outputs can be decomposed based on the ES as

$$\begin{aligned} V(\Delta) &= V_{\mathbf{ES}}E_{\sim\mathbf{ES}|\mathbf{ES}}(\Delta|\mathbf{ES}) + E_{\mathbf{ES}}V_{\sim\mathbf{ES}|\mathbf{ES}}(\Delta|\mathbf{ES}) \\ &= V_{\mathbf{ES}}E_{\mathbf{GC},\mathbf{HM},\mathbf{PA}|\mathbf{ES}}(\Delta|\mathbf{ES}) + E_{\mathbf{ES}}V_{\mathbf{GC},\mathbf{HM},\mathbf{PA}|\mathbf{ES}}(\Delta|\mathbf{ES}), \end{aligned} \tag{2}$$

where **ES** is the set of multiple alternative ESs, **GC** is the set of multiple GCs, **HM** is the set of multiple HMs, and $\mathbf{PA} = \mathbf{PA}^{(1)} \cup \mathbf{PA}^{(2)} \cdots \cup \mathbf{PA}^{(k)}$ is the PA set for all the models, with $\mathbf{PA}^{(k)}$ representing the PAs for a given model HM_k; $\sim$**ES** represents uncertainty sources, excluding **ES**, which are **GC**, **HM**, and **PA**. The subscripts **GC**, **HM**, **PA**|**ES** refer to the change in the GCs, HMs, and PA combinations under a fixed ES. The first and second terms on the right-hand side of Eq. (2) represent the partial variances contributed by alternative ESs and other uncertainty sources, respectively.

The partial variance caused by other uncertainty sources $V_{\mathbf{GC},\mathbf{HM},\mathbf{PA}|\mathbf{ES}}(\Delta|\mathbf{ES})$ can be further decomposed based on multiple plausible GCs as

$$\begin{aligned} V_{\mathbf{GC},\mathbf{HM},\mathbf{PA}|\mathbf{ES}}(\Delta|\mathbf{ES}) &= V_{\mathbf{GC}|\mathbf{ES}}E_{\sim\mathbf{GC}|\mathbf{GC},\mathbf{ES}}(\Delta|\mathbf{GC},\mathbf{ES}) + E_{\mathbf{GC}|\mathbf{ES}}V_{\sim\mathbf{GC}|\mathbf{GC},\mathbf{ES}}(\Delta|\mathbf{GC},\mathbf{ES}) \\ &= V_{\mathbf{GC}|\mathbf{ES}}E_{\mathbf{HM},\mathbf{PA}|\mathbf{GC},\mathbf{ES}}(\Delta|\mathbf{GC},\mathbf{ES}) + E_{\mathbf{GC}|\mathbf{ES}}V_{\mathbf{HM},\mathbf{PA}|\mathbf{GC},\mathbf{ES}}(\Delta|\mathbf{GC},\mathbf{ES}), \end{aligned} \tag{3}$$

where the first partial variance term on the right-hand side of this equation represents the uncertainty contributed by multiple plausible GCs. The subscripts **GC**|**ES** and **HM**, **PA**|**GC**, **ES** refer to the changes in GCs under one ES and the changes in HMs and PAs under one GC and ES, respectively. The second term represents the within-GC partial variance, which is caused by the HMs and PAs.

Following the same procedure, the partial variance $V_{\mathbf{HM},\mathbf{PA}|\mathbf{GC},\mathbf{ES}}(\Delta|\mathbf{GC},\mathbf{ES})$ can be further decomposed based on multiple HMs as

$$\begin{aligned} V_{\mathbf{HM,PA|GC,ES}}(\Delta|\mathbf{GC,ES}) &= V_{\mathbf{HM|GC,ES}}E_{\sim\mathbf{HM|HM,GC,ES}}(\Delta|\mathbf{HM,GC,ES}) \\ &\quad + E_{\mathbf{HM|GC,ES}}V_{\sim\mathbf{HM|HM,GC,ES}}(\Delta|\mathbf{HM,GC,ES}) \\ &= V_{\mathbf{HM|GC,ES}}E_{\mathbf{PA|HM,GC,ES}}(\Delta|\mathbf{HM,GC,ES}) \\ &\quad + E_{\mathbf{HM|GC,ES}}V_{\mathbf{PA|HM,GC,ES}}(\Delta|\mathbf{HM,GC,ES}), \end{aligned} \tag{4}$$

where the first term on the right-hand side of Eq. (4) represents the partial variance contributed by multiple plausible HMs. The subscripts **HM**|**GC**, **ES** and **PA**|**HM**, **GC**, **ES** refer to the change in HMs under one GC and one ES and the change in PAs under one HM, one GC, and one ES, respectively. The second term represents the within-HM partial variance, which is caused by the PAs. Therefore, the total variance in the model outputs can be decomposed as

$$\begin{aligned} V(\Delta) &= E_{\mathbf{ES}}V_{\mathbf{GC,HM,PA|ES|}}(\Delta|\mathbf{ES}) + V_{\mathbf{ES}}E_{\mathbf{GC|ES}}E_{\mathbf{HM|GC,ES}}E_{\mathbf{PA|HM,GC,ES}}(\Delta|\mathbf{ES}) \\ &= E_{\mathbf{ES}}[E_{\mathbf{GC|ES}}V_{\mathbf{HM,PA|GC,ES}}(\Delta|\mathbf{GC,ES}) + V_{\mathbf{GC|ES}}E_{\mathbf{HM,PA|GC,ES}}(\Delta|\mathbf{GC,ES})] \\ &\quad + V_{\mathbf{ES}}E_{\mathbf{GC|ES}}E_{\mathbf{HM|GC,ES}}E_{\mathbf{PA|HM,GC,ES}}(\Delta|\mathbf{ES}) \\ &= E_{\mathbf{ES}}E_{\mathbf{GC|ES}}E_{\mathbf{HM|GC,ES}}V_{\mathbf{PA|HM,GC,ES}}(\Delta|\mathbf{HM,GC,ES}) \\ &\quad + E_{\mathbf{ES}}E_{\mathbf{GC|ES}}V_{\mathbf{HM|GC,ES}}E_{\mathbf{PA|HM,GC,ES}}(\Delta|\mathbf{HM,GC,ES}) \\ &\quad + E_{\mathbf{ES}}V_{\mathbf{GC|ES}}E_{\mathbf{HM|GC,ES}}E_{\mathbf{PA|HM,GC,ES}}(\Delta|\mathbf{HM,GC,ES}) \\ &\quad + V_{\mathbf{ES}}E_{\mathbf{GC|ES}}E_{\mathbf{HM|GC,ES}}E_{\mathbf{PA|HM,GC,ES}}(\Delta|\mathbf{HM,GC,ES}) \\ &= V(\mathbf{PA}) + V(\mathbf{HM}) + V(\mathbf{GC}) + V(\mathbf{ES}), \end{aligned} \tag{5}$$

where $V(\mathbf{PA})$, $V(\mathbf{HM})$, $V(\mathbf{GC})$, and $V(\mathbf{ES})$ in Eq. (5), represent the variances contributed from four sources of input uncertainty: PA, HM, GC, and ES. Following the definition of the first-order sensitivity index, the new set of sensitivity indices for our HSAF can be defined as

$$\begin{aligned} S_{\mathbf{ES}} &= \frac{V_{\mathbf{ES}}E_{\mathbf{GC||S}}E_{\mathbf{HM|GC,ES}}E_{\mathbf{PA|HM,GC,ES}}(\Delta|\mathbf{HM,GC,ES})}{V(\Delta)} = \frac{V(\mathbf{ES})}{V(\Delta)} \\ S_{\mathbf{GC}} &= \frac{E_{\mathbf{ES}}V_{\mathbf{GC||S}}E_{\mathbf{HM|GC,ES}}E_{\mathbf{PA|HM,GC,ES}}(\Delta|\mathbf{HM,GC,ES})}{V(\Delta)} = \frac{V(\mathbf{GC})}{V(\Delta)} \\ S_{\mathbf{HM}} &= \frac{E_{\mathbf{ES}}E_{\mathbf{GC||S}}V_{\mathbf{HM|GC,ES}}E_{\mathbf{PA|HM,GC,ES}}(\Delta|\mathbf{HM,GC,ES})}{V(\Delta)} = \frac{V(\mathbf{HM})}{V(\Delta)} \\ S_{\mathbf{PA}} &= \frac{E_{\mathbf{ES}}E_{\mathbf{GC||S}}E_{\mathbf{HM|GC,ES}}V_{\mathbf{PA|HM,GC,ES}}(\Delta|\mathbf{HM,GC,ES})}{V(\Delta)} = \frac{V(\mathbf{PA})}{V(\Delta)}. \end{aligned} \tag{6}$$

2) THREE-LAYER HSAF

For the three-layer HSAF (without considering the HM uncertainty), the total variance can be decomposed (following the same process) as

$$\begin{aligned} V(\Delta) &= E_{\mathbf{ES}}V_{\mathbf{GC,PA|ES}}(\Delta|\mathbf{ES}) + V_{\mathbf{ES}}E_{\mathbf{GC|ES}}E_{\mathbf{PA|GC,ES}}(\Delta|\mathbf{ES}) \\ &= E_{\mathbf{ES}}[E_{\mathbf{GC|ES}}V_{\mathbf{PA|GC,ES}}(\Delta|\mathbf{GC,ES}) + V_{\mathbf{GC|ES}}E_{\mathbf{PA|GC,ES}}(\Delta|\mathbf{GC,ES})] \\ &\quad + V_{\mathbf{ES}}E_{\mathbf{GC|ES}}E_{\mathbf{PA|GC,ES}}(\Delta|\mathbf{ES}) \\ &= E_{\mathbf{ES}}E_{\mathbf{GC|ES}}V_{\mathbf{PA|GC,ES}}(\Delta|\mathbf{GC,ES}) + E_{\mathbf{ES}}V_{\mathbf{GC|ES}}E_{\mathbf{PA|GC,ES}}(\Delta|\mathbf{GC,ES}) \\ &\quad + V_{\mathbf{ES}}E_{\mathbf{GC|ES}}E_{\mathbf{PA|GC,ES}}(\Delta|\mathbf{GC,ES}) \\ &= V(\mathbf{PA}) + V(\mathbf{GC}) + V(\mathbf{ES}). \end{aligned} \tag{7}$$

The new set of sensitivity indices can be defined as

$$S_{\mathbf{ES}} = \frac{V_{\mathbf{ES}}E_{\mathbf{GC}|\mathbf{ES}}E_{\mathbf{PA}|\mathbf{GC},\mathbf{ES}}(\Delta|\mathbf{GC},\mathbf{ES})}{V(\Delta)} = \frac{V(\mathbf{ES})}{V(\Delta)}$$

$$S_{\mathbf{GC}} = \frac{E_{\mathbf{ES}}V_{\mathbf{GC}|\mathbf{ES}}E_{\mathbf{PA}|\mathbf{GC},\mathbf{ES}}(\Delta|\mathbf{GC},\mathbf{ES})}{V(\Delta)} = \frac{V(\mathbf{GC})}{V(\Delta)}$$

$$S_{\mathbf{PA}} = \frac{E_{\mathbf{ES}}E_{\mathbf{GC}|\mathbf{ES}}V_{\mathbf{PA}|\mathbf{GC},\mathbf{ES}}(\Delta|\mathbf{GC},\mathbf{ES})}{V(\Delta)} = \frac{V(\mathbf{PA})}{V(\Delta)}. \quad (8)$$

b. Calculation of sensitivity indices by LHS

A conventional approach for the variance estimation in Eqs. (6) and (8) is the Monte Carlo (MC) method (Song et al. 2015). However, conventional MC sampling is computationally expensive, especially for the high-dimensional models used in this study. LHS is one of the most popular random sampling methods due to its significantly faster convergence rate $[O(N^{-3})]$ than conventional MC $[O(N^{-1/2})]$ or quasi–Monte Carlo $[O(N^{-2/3})]$ (Dick et al. 2013; Iman and Conover 1980; Guth et al. 2019). To reduce the unaffordable computational cost, the LHS method was used to generate the random PA samples in this study (Helton and Davis 2003; McKay et al. 1979).

LHS divides the ranges of the m model parameters into n disjointed intervals with an equal probability $1/n$ from which one value is sampled randomly in each interval. Assuming that we have k alternative ESs, l plausible GCs under each ES, j plausible HMs under each GC and n LHS-generated PA sets, the partial variance caused by PA uncertainty can be estimated as

$$V(\mathbf{PA}) = E_{\mathbf{ES}}E_{\mathbf{GC}|\mathbf{ES}}E_{\mathbf{HM}|\mathbf{GC},\mathbf{ES}}V_{\mathbf{PA}|\mathbf{HM},\mathbf{GC},\mathbf{ES}}(\Delta|\mathbf{HM},\mathbf{GC},\mathbf{ES})$$
$$= \sum_k\sum_l\sum_j \left\{ \begin{array}{l} \frac{1}{n}\sum_{i=1}^{n}\Delta^2(\mathrm{PA}_i|\mathrm{HM}_j,\mathrm{GC}_l,\mathrm{ES}_k) \\ -\left[\frac{1}{n}\sum_{i=1}^{n}\Delta(\mathrm{PA}_i|\mathrm{HM}_j,\mathrm{GC}_l,\mathrm{ES}_k)\right]^2 \end{array} \right\} P(\mathrm{HM}_j|\mathrm{GC}_l,\mathrm{ES}_k)P(\mathrm{GC}_l|\mathrm{ES}_k)P(\mathrm{ES}_k), \quad (9)$$

where $P(\mathrm{HM}_j|\mathrm{GC}_l,\mathrm{ES}_k)$ is the weight of model HM_j under GC_l and ES_k satisfying $\sum_j P(\mathrm{HM}_j|\mathrm{GC}_l,\mathrm{ES}_k) = 1$, $P(\mathrm{GC}_l|\mathrm{ES}_k)$ is the weight of GC_l satisfying $\sum_l P(\mathrm{GC}_l|\mathrm{ES}_k) = 1$, and $P(\mathrm{ES}_k)$ is the weight of ES_k satisfying $\sum_k P(\mathrm{ES}_k) = 1$. Similarly, the partial variances of the HMs, GCs and ESs can be calculated as

$$V(\mathbf{HM}) = E_{\mathbf{ES}}E_{\mathbf{GC}|\mathbf{ES}}V_{\mathbf{HM}|\mathbf{GC},\mathbf{ES}}E_{\mathbf{PA}|\mathbf{HM},\mathbf{GC},\mathbf{ES}}(\Delta|\mathbf{HM},\mathbf{GC},\mathbf{ES})$$
$$= E_{\mathbf{ES}}E_{\mathbf{GC}|\mathbf{ES}}\left\{ \begin{array}{l} E_{\mathbf{HM}|\mathbf{GC},\mathbf{ES}}\left[E_{\mathbf{PA}|\mathbf{HM},\mathbf{GC},\mathbf{ES}}(\Delta|\mathbf{HM},\mathbf{GC},\mathbf{ES})\right]^2 \\ -\left[E_{\mathbf{HM}|\mathbf{GC},\mathbf{ES}}E_{\mathbf{PA}|\mathbf{HM},\mathbf{GC},\mathbf{ES}}(\Delta|\mathbf{HM},\mathbf{GC},\mathbf{ES})\right]^2 \end{array} \right\}$$
$$= \sum_k P(\mathrm{ES}_k)\sum_l P(\mathrm{GC}_l|\mathrm{ES}_k)\left\{ \begin{array}{l} \sum_j\left[\frac{1}{n}\sum_{i=1}^{n}\Delta(\mathrm{PA}_i|\mathrm{HM}_j,\mathrm{GC}_l,\mathrm{ES}_k)\right]^2 P(\mathrm{HM}_j|\mathrm{GC}_l,\mathrm{ES}_k) \\ -\sum_j\left[\frac{1}{n}\sum_{i=1}^{n}\Delta(\mathrm{PA}_i|\mathrm{HM}_j,\mathrm{GC}_l,\mathrm{ES}_k)P(\mathrm{HM}_j|\mathrm{GC}_l,\mathrm{ES}_k)\right]^2 \end{array} \right\}, \quad (10)$$

$$V(\mathbf{GC}) = E_{\mathbf{ES}}V_{\mathbf{GC}|\mathbf{ES}}E_{\mathbf{HM}|\mathbf{GC},\mathbf{ES}}E_{\mathbf{PA}|\mathbf{HM},\mathbf{GC},\mathbf{ES}}(\Delta|\mathbf{HM},\mathbf{GC},\mathbf{ES})$$
$$= E_{\mathbf{ES}}\left\{ \begin{array}{l} E_{\mathbf{GC}|\mathbf{ES}}\left[E_{\mathbf{HM}|\mathbf{GC},\mathbf{ES}}E_{\mathbf{PA}|\mathbf{HM},\mathbf{GC},\mathbf{ES}}(\Delta|\mathbf{HM},\mathbf{GC},\mathbf{ES})\right]^2 \\ -\left[E_{\mathbf{GC}|\mathbf{ES}}E_{\mathbf{HM}|\mathbf{GC},\mathbf{ES}}E_{\mathbf{PA}|\mathbf{HM},\mathbf{GC},\mathbf{ES}}(\Delta|\mathbf{HM},\mathbf{GC},\mathbf{ES})\right]^2 \end{array} \right\}$$
$$= \sum_k P(\mathrm{ES}_k)\left(\begin{array}{l} \sum_j P(\mathrm{GC}_l|\mathrm{ES}_k)\left\{\sum_j\left[\frac{1}{n}\sum_{i=1}^{n}\Delta\left(\mathrm{PA}_i|\mathrm{HM}_j,\mathrm{GC}_l,\mathrm{ES}_k\right)\right]P\left(\mathrm{HM}_j|\mathrm{GC}_l,\mathrm{ES}_k\right)\right\}^2 \\ -\left\{\sum_l\sum_j P(\mathrm{GC}_l|\mathrm{ES}_k)P(\mathrm{HM}_j|\mathrm{GC}_l,\mathrm{ES}_k)\left[\frac{1}{n}\sum_{i=1}^{n}\Delta\left(\mathrm{PA}_i|\mathrm{HM}_j,\mathrm{GC}_l,\mathrm{ES}_k\right)\right]\right\}^2 \end{array} \right), \quad (11)$$

TABLE 1. Basic information on the selected 20 CMIP5 models.

Modeling name	Institution	Resolution (°)
BCC-CSM1.1	Beijing Climate Centre, China	2.8 × 2.8
BCC-CSM1.1-m	Beijing Climate Centre, China	2.8 × 2.8
CanESM2	Canadian Centre for Climate Modeling and Analysis, Canada	2.8 × 2.8
CCSM4	National Centre for Atmospheric Research, United States	1.25 × 0.94
CNRM-CM5	Centre National de Recherches Meteorologiques	1.4 × 1.4
CSIRO-Mk3.6.0	Australian Commonwealth Scientific and Industrial Research Organisation in collaboration with the Queensland Climate Change Centre of Excellence, Australia	1.875 × 1.875
FGOALS-g2	Institute of Atmospheric Physics, Chinese Academy of Sciences, and Tsinghua University, China	2.8 × 2.8
GFDL-CM3	NOAA Geophysical Fluid Dynamics Laboratory, United States	2.5 × 2.0
GFDL-ESM2G		
GFDL-ESM2M		
HadGEM2-ES	Met Office Hadley Centre	1.875 × 1.25
IPSL-CM5A-LR	Institute Pierre-Simon Laplace, France	1.9 × 3.75
IPSL-CM5A-MR		2.5 × 1.25
MIROC5	Atmosphere and Ocean Research Institute (The University of Tokyo), National Institute for Environmental Studies, and Japan Agency for Marine-Earth Science and Technology, Japan	1.4 × 1.4
MIROC-ESM-CHEM		2.8 × 2.8
MIROC-ESM		2.8 × 2.8
MPI-ESM-LR	Max Planck Institute for Meteorology, Germany	1.875 × 1.875
MPI-ESM-MR		1.875 × 1.875
MRI-CGCM3	Meteorological Research Institute, Japan	1.1 × 1.1
NorESM1-M	Norwegian Climate Centre, Norway	2.5 × 1.875

$$
\begin{aligned}
V(\mathbf{ES}) &= V_{\mathbf{ES}} E_{\mathbf{GC}|\mathbf{ES}} E_{\mathbf{HM}|\mathbf{GC},\mathbf{ES}} E_{\mathbf{PA}|\mathbf{HM},\mathbf{GC},\mathbf{ES}}(\Delta|\mathbf{HM},\mathbf{GC},\mathbf{ES}) \\
&= E_{\mathbf{ES}}\left[E_{\mathbf{GC}|\mathbf{ES}} E_{\mathbf{HM}|\mathbf{GC},\mathbf{ES}} E_{\mathbf{PA}|\mathbf{HM},\mathbf{GC},\mathbf{ES}}(\Delta|\mathbf{GC})\right]^2 - \left[E_{\mathbf{ES}} E_{\mathbf{GC}|\mathbf{ES}} E_{\mathbf{HM}|\mathbf{GC},\mathbf{ES}} E_{\mathbf{PA}|\mathbf{HM},\mathbf{GC},\mathbf{ES}}(\Delta|\mathbf{GC})\right]^2 \\
&= \sum_k P(\mathrm{ES}_k)\left(\sum_l \sum_j P(\mathrm{GC}_l|\mathrm{ES}_k) P(\mathrm{HM}_j|\mathrm{GC}_l,\mathrm{ES}_k)\left[\frac{1}{n}\sum_{i=1}^{n}\Delta\left(\mathrm{PA}_i|\mathrm{HM}_j,\mathrm{GC}_l,\mathrm{ES}_k\right)\right]\right)^2 \\
&\quad - \left\{\sum_k \sum_l \sum_j P(\mathrm{ES}_k) P(\mathrm{GC}_l|\mathrm{ES}_k) P(\mathrm{HM}_j|\mathrm{GC}_l,\mathrm{ES}_k)\left[\frac{1}{n}\sum_{i=1}^{n}\Delta\left(\mathrm{PA}_i|\mathrm{HM}_j,\mathrm{GC}_l,\mathrm{ES}_k\right)\right]\right\}^2 .
\end{aligned}
\tag{12}
$$

Based on Eqs. (9)–(12), the sensitivity indices defined in Eq. (6) (four-layer HSAF) and Eq. (8) (three-layer HSAF) can be evaluated.

c. GCs and ESs

ESs provide plausible descriptions of how the world might evolve during the twenty-first century with respect to a range of variables, such as technological change, socioeconomic change, energy and land use, and emissions of greenhouse gases and air pollutants (van Vuuren et al. 2011). GCs driven by a time series of ESs are considered the most essential and feasible tools for making projections of future climate change and have been widely applied to evaluate the hydrological impacts of climate change (Kay et al. 2009; Habets et al. 2013; Xu et al. 2013; Alfieri et al. 2015; Wu et al. 2014, 2015). In this study, daily precipitation data and maximum and minimum temperature data from 20 GCs provided by the CMIP5 (https://esgf-node.llnl.gov/search/cmip5/) were used (Table 1). We chose these 20 GCs because they have both daily data and three representative concentration pathways (RCP2.6, RCP4.5, and RCP8.5). The period 1971–2000 was chosen as the baseline period for BRB, while the period 1979–2005 was chosen as the baseline period for LRB (due to the observational data beginning in 1979). The period 2071–2100 under three ESs (RCP2.6, RCP4.5, and RCP8.5) was considered the future period for both basins.

For bias correction, the GC outputs (i.e., temperature and precipitation) were first rescaled to high spatial resolutions (0.25° for BRB and 0.5° for LRB) over the study basins using the nearest interpolation method, and then, the variance-based change factor (VB-CF) methodology was used to correct the biases in temperature and precipitation simulations for each GC based on the observed gridded dataset (see section 3b). The VB-CF method is based on matching two distributions with the same shape to model historical and future simulations (Hawkins et al. 2013; Wang et al. 2016). The daily precipitation and temperature of the models can be corrected as

$$
X_{\mathrm{adj,fut}}(t) = \overline{X_{\mathrm{raw}}} + \frac{\sigma_{X,\mathrm{raw}}}{\sigma_{X,\mathrm{ref}}}\left[X_{\mathrm{obs}}(t) - \overline{X_{\mathrm{ref}}}\right]. \tag{13}
$$

where $\overline{X_{\mathrm{raw}}}$ and $\sigma_{X,\mathrm{raw}}$ represent the long-term average and standard deviation of the future simulations, respectively; $\overline{X_{\mathrm{ref}}}$ and $\sigma_{X,\mathrm{ref}}$ are the long-term average and standard deviation of

the present simulations, respectively. According to Eq. (13), the bias-corrected precipitation and temperature of 20 GCs during the present (reference) period (1971–2000 for BRB and 1979–2005 for LRB) are the same as the observations.

d. HMs and PAs

Two physically based distributed HMs (VIC and CREST) and a lumped conceptual HM (Xinanjiang) are used to investigate the contributions of HM and PA to the overall uncertainty in hydrological projections, because these three models are good at representing HMs with different levels of complexity and structure.

1) VIC MODEL

The VIC model is a semidistributed grid-based HM that was developed by the University of Washington and Princeton University. The model can simulate the physical exchange of water and energy among the atmosphere, soil, and vegetation in a surface vegetation–atmospheric transfer scheme (Liang et al. 1994; Lohmann et al. 1998). In this study, version 4.1.2d of the VIC model (www.hydro.washington.edu/Lettenmaier/Models/VIC/index.shtml) was run to simulate the water balance over the two study basins. The Dag Lohmann model (Nijssen et al. 1997) was used to transport the grid cell surface runoff and baseflow simulated by the VIC model within each grid cell to the outlet of the grid cell and then into the river system. Seven PAs needed to be calibrated in the VIC model (Table S1 in the online supplemental material). The PA SA of the VIC model has been demonstrated by Demaria et al. (2007) in four catchments in the U.S. and by Gou et al. (2020) in 10 major river basins across China, both of which suggest that the infiltration curve shape parameter (B) and the soil depths of layers 1 (d_1) and 2 (d_2) are the most sensitive PAs. The parameter B represents the relative area ratio of the average water content of the grid to the maximum water content of the grid. A larger B indicates greater inhomogeneity of the spatial distribution of the moisture content and more surface runoff. Meanwhile, changes in d_1 and d_2 affect soil evapotranspiration, which further influences surface and subsurface runoff. Therefore, these three PAs (B, d_1, and d_2) were chosen for uncertainty analysis in this study. The ranges of the PAs were chosen based on the minimum and maximum parameter values in the Global Land Data Assimilation Systems (GLDAS) dataset for China (Table S1).

2) CREST MODEL

CREST is a grid-based distributed HM developed by the University of Oklahoma and NASA SERVIR. The model can simulate the spatial and temporal variations of land surface and subsurface water fluxes and storages by cell-to-cell simulation. The details of the CREST model can be found in Wang et al. (2011). In this study, version 2.1.2 of CREST is used to simulate the discharge at the outlet of the two basins (Tang et al. 2016). Table S1 shows 12 PAs of the CREST model and their ranges. We screened the most sensitive PAs of the CREST model by using the Morris method (see section 2e). The ranges of the PAs are determined based on the work of Wang et al. (2011) and Xue et al. (2013).

3) XINANJIANG MODEL

The Xinanjiang model is a conceptual rainfall–runoff HM developed by Zhao et al. (1980). In this HM, actual evapotranspiration is computed from potential evapotranspiration, while the soil storage deficit is represented in three layers, i.e., upper, lower, and deep soil layers. The total runoff is divided into surface runoff, interflow and groundwater runoff using a free water capacity distribution curve and is estimated using a soil moisture storage capacity distribution curve based on the concept of the effect of runoff formation on repletion of storage. Surface runoff is routed by the lag-and-route method, while interflow and groundwater are routed through linear reservoirs representing interflow and groundwater storage, respectively (Zhao 1992; Zhao and Liu 1995). This model has been widely used in many regions of the world (Lin et al. 2014; Liu et al. 2009; Yao et al. 2014). There are 12 PAs in the Xinanjiang model (see Table S1). Among these parameters, four PAs (the areal mean free water capacity of the surface soil layer, SM; the recession constant of surface water storage, CS; the ratio of potential evapotranspiration to pan evaporation, K_C; and the outflow coefficients of the free water storage to groundwater relationships, KG) play a vital role in model calibration (Ren et al. 2010). We screened the most sensitive PAs of the Xinanjiang model by using the Morris method (see section 2e). The ranges of the parameters are determined based on previous studies (Ren et al. 2010; Song et al. 2013; Wang and Zhao 1989; Zhao 1992).

e. Screening procedure for sensitive PAs

Considering the large number of PAs in the three HMs, the Morris method was used to screen the most sensitive PAs before performing uncertainty analysis (Morris 1991). The principle of the Morris method is the discretization of each input PA in levels and the implementation of a number of OAT designs, in which each PA is varied while others are fixed. The selection of the variation direction and the samples from the PA space is random. The elementary effects of each PA on the model output are estimated by repeating these steps.

The number of OAT designs is denoted as n, and the PA space is divided into P levels. Here $\mathrm{EE}_i^{(j)}$, the elementary effect of the ith input PA at the jth repetition, is expressed as follows:

$$\mathrm{EE}_i^{(j)} = \frac{y\left(\boldsymbol{\theta}^{(j)} + \triangle \mathbf{e}_i\right) - y\left(\boldsymbol{\theta}^{(j)}\right)}{\beta}, \tag{14}$$

where $\beta = 1/(P-1)$ and $\mathbf{e}_i$ is a vector of the canonical base. The evaluation indices are obtained as follows:

$$\mu_i^* = \frac{\left(\sum_{j=1}^{n} |\mathrm{EE}_i^{(j)}|\right)}{n}, \tag{15}$$

$$\sigma_i = \sqrt{\frac{\sum_{j=1}^{n}\left[\mathrm{EE}_i^{(j)} - \left(\sum_{j=1}^{n}\mathrm{EE}_i^{(j)}\right)\Big/ n\right]^2}{n}}. \tag{16}$$

where μ_i^* is a measure of the influence of the ith PA on the model output. A larger μ_i^* represents a larger uncertainty

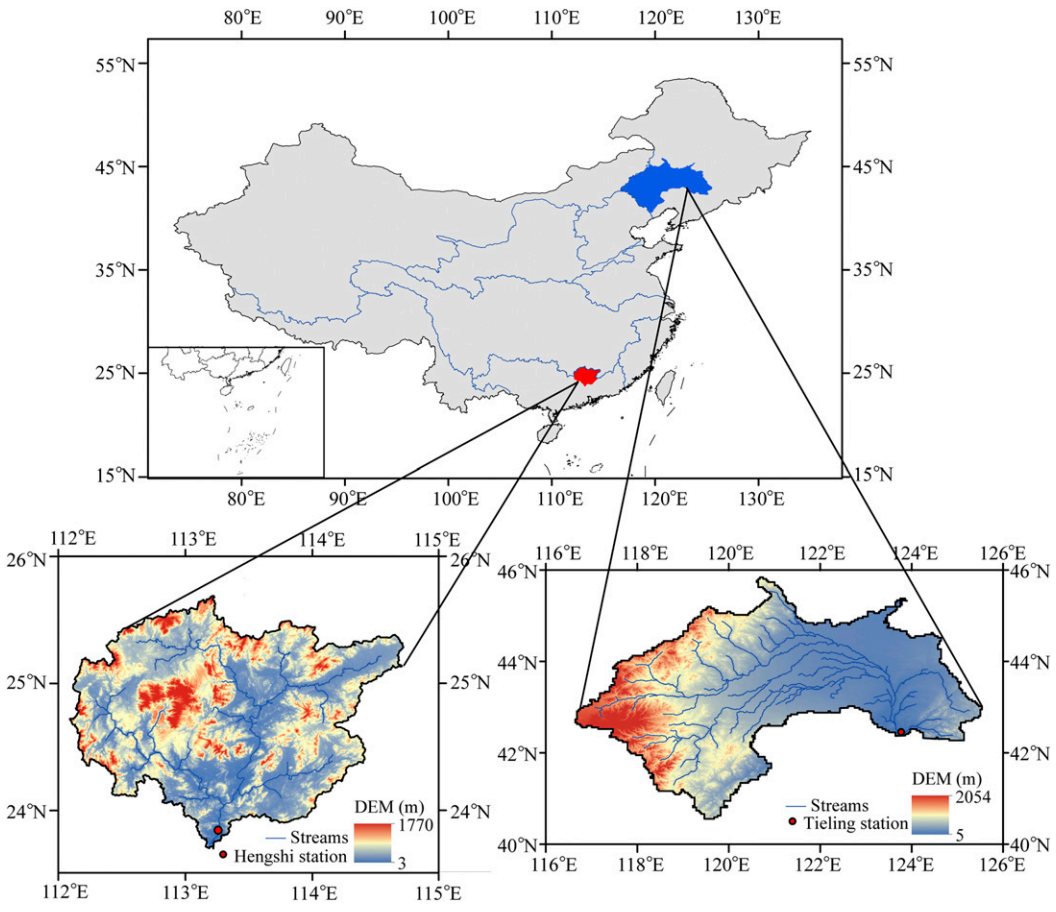

FIG. 2. Map showing the location of the study basins and hydrological stations.

contribution of the ith PA to the model output, and vice versa. The term σ_i is a measure of the interaction effects between PAs. A larger σ_i suggests stronger interaction effects between PAs.

3. Study area and datasets

a. Study area

The BRB is the second largest tributary of the Pearl River in southern China. The study area accounts for 73% of the BRB and has a drainage area of 34 097 km^2 (Fig. 2). The BRB is located in tropical and subtropical climate zones, with precipitation during the flood season (April–September) accounting for approximately 70%–80% of the annual precipitation. Due to sufficient precipitation, its high humidity and climate warming, the BRB has often suffered extreme floods (e.g., June and August 1994, June 1998, June 2005, and July 2006) in the past few decades and will likely encounter more severe floods in the next few decades (Wu et al. 2014, 2015).

The LRB is located in northeast China and has a drainage area of 12.1 $\times$ 10^4 km^2 (Fig. 2). Most of the LRB is characterized by a semiarid monsoon climate, with an annual average temperature from 4° to 9°C and an annual average precipitation between 350 and 1000 mm. Intra-annual precipitation is unevenly distributed, and precipitation from June to September accounts for more than 70% of the annual precipitation. The Hengshi and Tieling hydrological stations are the discharge stations of the BRB and LRB, respectively (Fig. 2).

b. Datasets

DEM data with a spatial resolution of 90 m were provided by the International Scientific and Technical Data Mirror Site, Computer Network Information Center, Chinese Academy of Sciences (http://datamirror.csdb.cn). The global 1-km land cover classification dataset was obtained from the University of Maryland (Hansen et al. 2000). The classification of the soil texture (at a resolution of 1 km) based on the Harmonized World Soil Database (HWSD) was provided by the Food and Agriculture Organization of the United Nations and the International Institute for Applied Systems Analysis.

For the BRB, the 30-yr (1971–2000) daily precipitation data from 24 rainfall stations and daily maximum and minimum temperature data from four meteorological stations (Table S2) were provided by the Hydrology Bureau of Guangdong Province and the China Meteorological Administration (http://cdc.cma.gov.cn/home.do), respectively. For the LRB, the high spatial resolution (0.1° $\times$ 0.1°) daily precipitation and temperature grid data for the period 1979–2007 were extracted

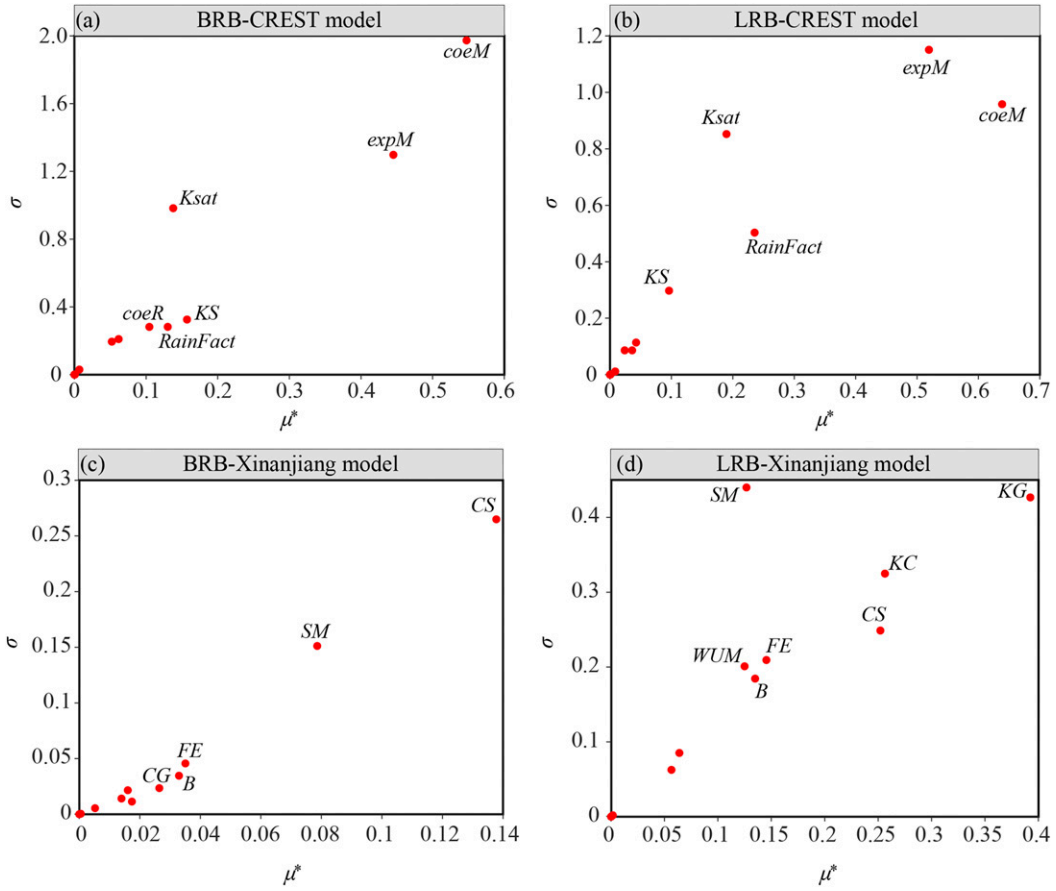

FIG. 3. Morris method outputs for the PAs of the CREST and Xinanjiang models in the BRB and LRB.

from the China Meteorological Forcing Dataset (He et al. 2020). The daily discharge data of the Hengshi (1971–2000) and Tieling (1996–2007) hydrological stations were provided by the Hydrological Bureau of the Ministry of Water Resources of China.

4. Results

a. Screening of sensitive PAs

The most sensitive PAs to the outputs of CREST and Xinanjiang are identified using the Morris method. Figure 3 shows the Morris outputs of the PAs in the two study basins. For the CREST model, coeM and expM are the two most sensitive PAs for both the BRB and LRB. For the Xinanjiang model, SM and CS are the two most sensitive PAs for the BRB, while K_C, KG, and CS are the three most sensitive PAs for the LRB. Therefore, coeM and expM of the CREST model; SM, CS, K_C, and KG of the Xinanjiang model; and B, d_1, and d_2 of the VIC model are selected to explore the uncertainty of PAs in terms of their climate hydrological impacts (Table 2). The LHS method is used to generate 20 samples for each selected PA of the three HMs (VIC, CREST, and Xinanjiang). We assume that the selected PAs follow a uniform or normal distribution (Table 2).

b. Hydrological simulations and predictions

For the BRB, the HM simulations are evaluated by dividing the recorded data series into three subperiods: 1970 for model warm-up, 1971–1990 for model calibration and 1991–2000 for model validation. For the LRB, 1995, 1996–2002, and 2003–07 are used for model warm-up, model calibration and validation, respectively. The efficacy of the HM simulations is evaluated using the Nash–Sutcliffe efficiency (NSE) coefficient and relative error (RE). The performance statistics for the three HMs in the two study basins are summarized in Table 3.

TABLE 2. Sensitive parameter used for three HMs; U represents uniform distribution, and N represents normal distribution.

Model	Parameter	Parameter range	Distribution
VIC	B	0–0.4	$B \sim U(0, 0.4)$
	d_1	0.01–0.5	$d_1 \sim U(0.01, 0.5)$
	d_2	0.05–1.0	$d_2 \sim U(0.05, 1.0)$
CREST	ExpM	0.1–2	expM $\sim U(0.1, 2)$
	CoeM	1–150	coeM $\sim U(90, 24.766)$
Xinanjiang	K_C	0.5–1.5	$K_C \sim N(1, 0.167)$
	CS	0–1	CS $\sim U(0, 1)$
	SM	0–100	SM $\sim N(50, 16.63)$
	KG	0.01–0.69	KG $\sim U(0.01, 0.69)$

TABLE 3. Model evaluation of discharge simulation at Hengshi station in the BRB and at Tieling station in the LRB.

Model	Period	Time scale	BRB		LRB	
			NSE	RE (%)	NSE	RE (%)
VIC	Calibration	Monthly	0.93	−3.8	0.91	11.5
		Daily	0.85		0.82	
	Validation	Monthly	0.91	−8.72	0.80	17.1
		Daily	0.82		0.63	
CREST	Calibration	Monthly	0.87	11.02	0.85	−19.9
		Daily	0.71		0.79	
	Validation	Monthly	0.88	4.36	0.72	13.6
		Daily	0.70		0.71	
Xinanjiang	Calibration	Monthly	0.87	2.36	0.85	−12.1
		Daily	0.75		0.78	
	Validation	Monthly	0.83	3.59	0.61	−16.0
		Daily	0.71		0.45	

For the BRB, the performance of the three HMs is satisfactory, with the NSE larger than 0.7 and RE less than 11% in both the calibration and validation periods. For the LRB, the VIC and CREST models perform relatively well, with NSE values greater than 0.63 and absolute RE values less than 20% during the calibration and validation periods, while the performance of the Xinanjiang model is relatively low in the validation period, mainly due to the lumped model structure and excess storage runoff mechanism. Overall, the simulated discharge is generally in good agreement with the observations, especially on the monthly time scale (Figs. S1 and S2 in the online supplemental material), suggesting that the selected HMs can reasonably reproduce the water balance of the two basins and can therefore be used to assess the hydrological impacts of future climate change.

Based on the HM simulations, we use 20 GCs under 3 different ESs to predict the future river discharge at the Hengshi (BRB) and Tieling (LRB) hydrological stations. Each HM was run on 20 sets of the selected PAs (see section 4a). For each basin, a total of 400 (20×20) simulation samples were generated for three HMs under each ES, so the total number of simulations was 3600 ($3 \times 3 \times 400$). Figure 4 displays the uncertainty range of the intra-annual discharges during the future period 2071–2100 from 3 HMs, 20 PAs, 20 GCs, and 3 ESs in the two study basins. There are significant differences in the average discharge projections between different simulation sample combinations of ESs, GCs, and PAs. For the BRB, the uncertainty range for each HM is larger in spring and summer (March–August) and smaller in autumn and winter (September–February). For the LRB, the uncertainty range for each HM is larger in summer and early autumn (June–October) and smaller in late autumn, winter, and spring (November–May). Furthermore, the uncertainty range tends to be larger under the highest ES (RCP8.5) for all the HMs in both basins.

c. *SA for river discharge at interannual and intra-annual scales*

Figure 5 displays the interannual variability (2071–2100) of the sensitivity indices of different ESs, GCs, HMs and PAs to the annual discharge projections at the Hengshi (BRB) and Tieling (LRB) stations. The sensitivity indices of the four sources of uncertainty show significantly larger interannual variability in the LRB than in the BRB, suggesting a stronger temporal variation in uncertainty in more arid climates. Overall, the ES is the least important source of uncertainty for the discharge predictions for both basins, with average contributions (sensitivity indices) of 0.9% and 1.4% for the BRB and LRB, respectively (Figs. 5a,e). This is well supported by Figs. S3a and S3e, which shows small discrepancies in the discharge projections among the three ESs. The HM and PA are generally the first and second largest uncertainty sources for the BRB on the interannual scale, with average contributions of 43.6% and 38.5%, respectively (Figs. 5c,d). For the LRB, the PA and HM are generally the first and second largest uncertainty sources, with average contributions of 68.7% and 23.6%, respectively (Figs. 5g,h). The GC is the third largest source of uncertainty for both basins and tends to be larger in the BRB (<34%, Fig. 5b) than in the LRB (<16.2%, Fig. 5f).

Figure 6 displays the intra-annual variability of the sensitivity indices of different ESs, GCs, HMs and PAs to the discharge projections in the two study basins. As shown, the uncertainties of the ES and GC tend to increase from January to June and decrease from June to December for the BRB (Figs. 6a,b), whereas the opposite patterns are identified for the uncertainties of the HM and PA (Figs. 6c,d), which is well supported by Figs. S4a and S4b. Overall, the HM and PA are the two most important sources of uncertainty in the BRB. The HM contributes large uncertainty (>51.6%) during late summer (August), autumn (September–November) and winter (December–February) and relatively small uncertainty (<38.9%) during spring (March–May) and early summer (June–July). The PA contributes larger uncertainty (>45.9%) during spring compared with the other seasons. The uncertainties of ES and GC first increase from January to June and then decrease from July to December (Figs. 6a,b), with large contributions during spring (1.3% and 14.2%) and summer (2% and 23.8%).

The intra-annual variability of the sensitivity indices in the LRB is significantly different from that in the BRB. For the LRB, the PA dominates the uncertainty in all months (>60%). The HM is the second-largest source of uncertainty, with average contributions of 27.7%, 17.3%, 15.9%, and 11.9% in

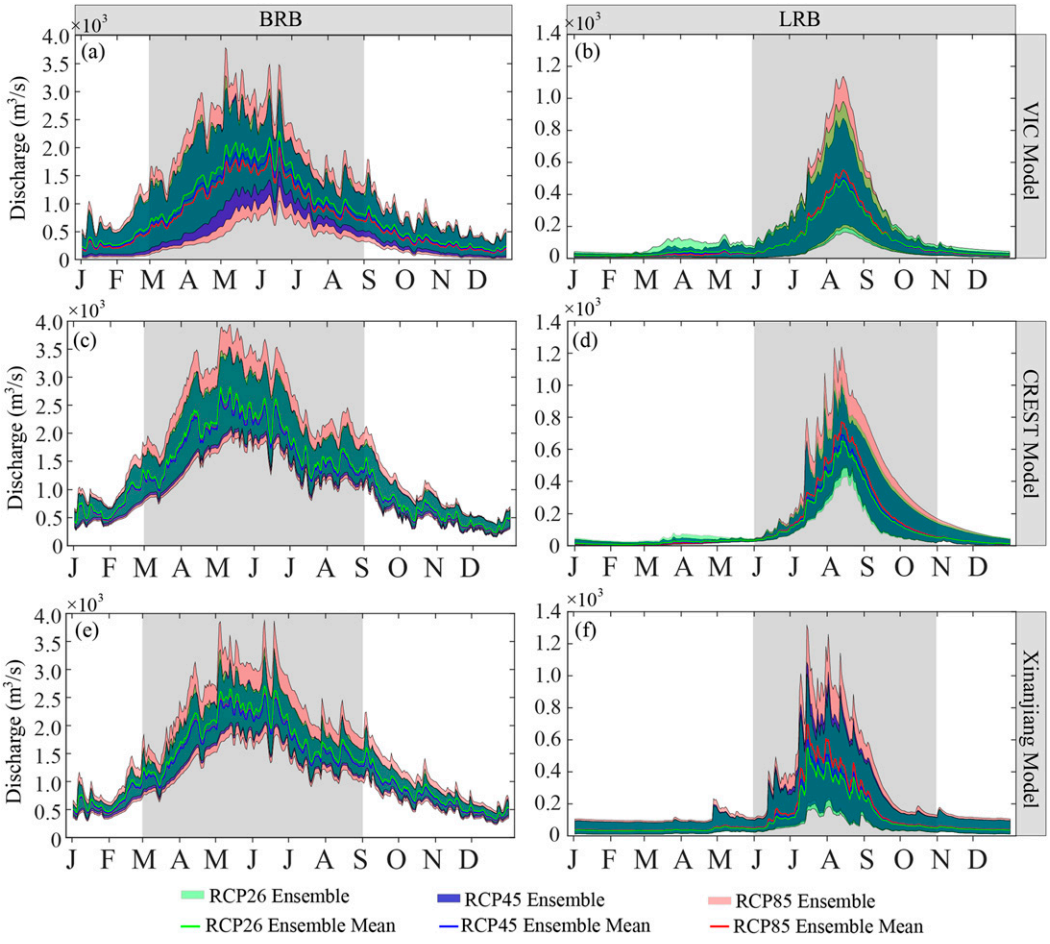

FIG. 4. Projections of the intra-annual discharge in the future period 2071–2100 by the VIC, CREST, and Xinanjiang models using 20 PAs, 20 GCs, and 3 different ESs in the BRB and LRB. The shaded area and the line represent ensemble simulations and ensemble average simulations, respectively, for a certain HM (VIC, CREST, or Xinanjiang).

winter, spring, summer, and autumn, respectively. The ES and GC contribute small uncertainties during May–June, late autumn (October–November) and winter, with average contributions of 0.08% and 2.9%, respectively, while the large uncertainties of ES and GC are found during March–April and July–September, with average contributions of 1.5% and 7.2%, respectively.

d. SA of annual peak discharge

Figure 7 displays the interannual variability of the sensitivity indices of the four uncertainty sources for the annual peak discharge (indicated by the annual maximum discharge) projections in the two study basins during the future period 2071–2100. As shown, the PA accounts for the largest uncertainty in the annual peak discharge projections for both basins, with average contributions of 78.7% and 76% in the BRB and LRB, respectively (Figs. 7d,h). In addition, the PA contributes greater uncertainty in the projections of the annual peak discharge compared with the annual discharge for both the BRB and LRB (Fig. 5), which suggests that the PA has a greater impact on the projections of extreme hydrological events.

Compared with PA, the uncertainty of HM tends to be smaller and accounts for 3%–22.6% of the total uncertainty in the BRB (Fig. 7), which is significantly smaller than contribution of the uncertainty of HM in the annual average discharge projections (26.1%–53.6%, Fig. 5). Compared with the BRB, the uncertainty of HM shows stronger variations in the LRB (1.1%–61.4%). Furthermore, the uncertainty of GC is larger in the BRB (4%–36.5%) than in the LRB (0.3%–8.9%). The ES remains the least important source of uncertainty, accounting for 0.2%–2.0% and 0.1%–2.9% of the total uncertainty for the BRB and LRB, respectively, which is smaller than its contribution to the total uncertainty in the BRB and LRB for the interannual projections (Fig. 5).

e. SA of surface runoff simulated by the VIC model

Based on the surface runoff simulations by the VIC model, the SA of three uncertainty sources (the ES, GC, and PA from the VIC model) for the surface runoff projections is conducted

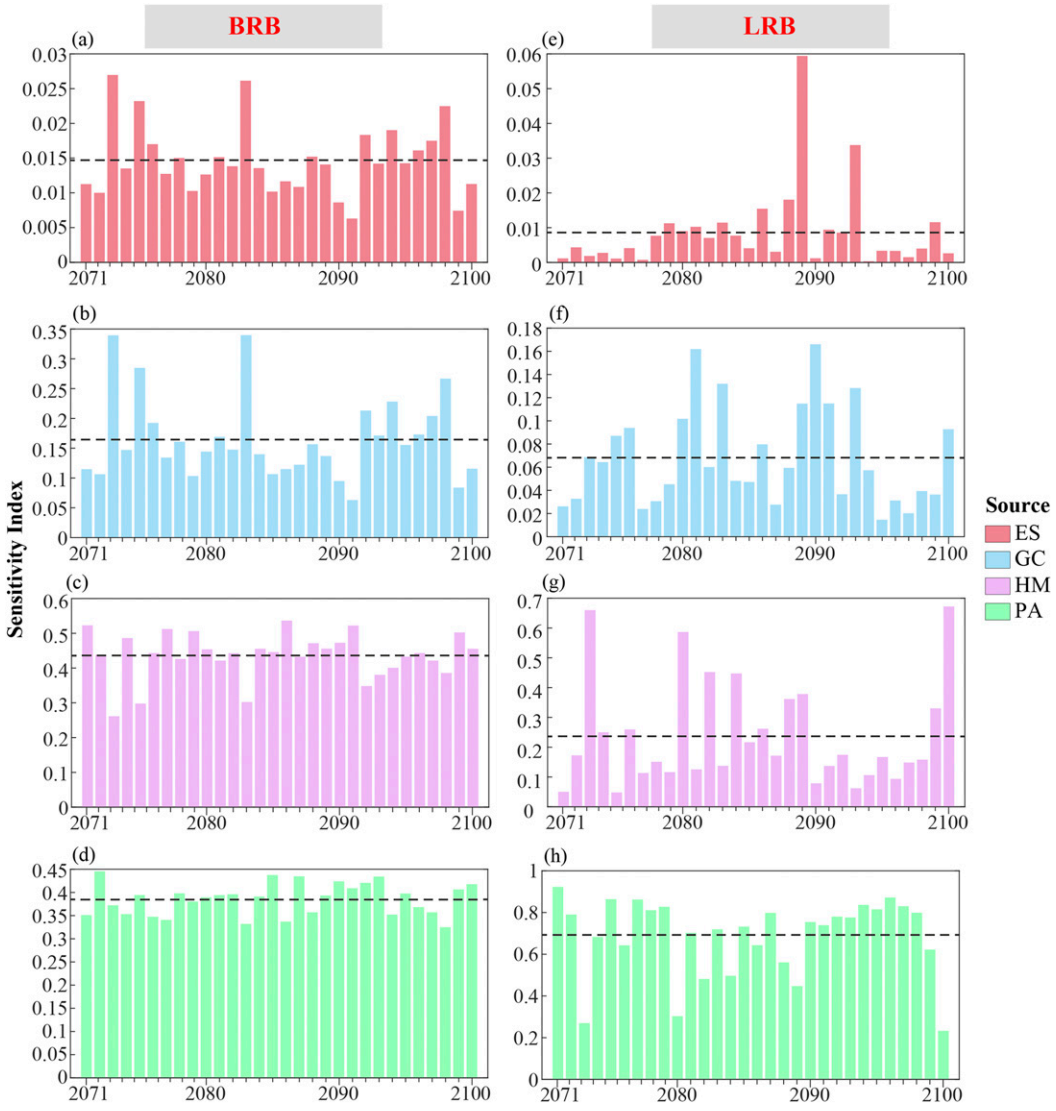

FIG. 5. Interannual variability of the sensitivity indices of the PA, HM, GC, and ES for the projected annual discharge at Hengshi station in the BRB and at Tieling station in the LRB in the future period 2071–2100. The sensitivity indices are calculated based on the four-layer HSAF [Eq. (6)].

in the two basins using the three-layer HSAF [i.e., Eqs. (7) and (8)]. Figure 8 displays the interannual and intra-annual variabilities (2071–2100) of the sensitivity indices of the ES, GC, and PA for the projections of the basin-averaged annual surface runoff over the two basins. On the interannual scale (Figs. 8a,b), the PA is the dominant contributor of uncertainty, accounting for 91.4% and 95.9% of the total uncertainty in the BRB and LRB, respectively. In contrast, the ES is the least important source of uncertainty for both basins, with a larger uncertainty in the BRB (0.6%–2.5%) than in the LRB (0.01%–1%). Similarly, the uncertainty of GC is significantly larger in the BRB (6.1%–31%) than in the LRB (2.2%–5.7%).

On the intra-annual scale (Fig. 8c), the uncertainty of PA decreases from January to June and increases from July to December in the BRB, with the largest and smallest uncertainty in December (94%) and June (89%), respectively, which is somewhat different from the uncertainty of PA at the four-layer HSAF (Fig. 6d). In contrast, the opposite pattern is identified for GC uncertainty, that is, the largest and smallest contributions of GC are detected in June (10.6%) and December (4.6%), respectively, similar to the GC uncertainty under the four-layer HSAF (Fig. 6b). For the LRB (Fig. 8d), the uncertainty of PA is dominant in all months and tends to be smaller in winter (80%), which is similar to the PA uncertainty under the four-HSAF (Fig. 6h). In contrast, the GC contributes larger uncertainty in winter (18%) than in the other seasons (5%), which is different from the uncertainty of GC under the four-layer HSAF, which had the smallest contribution in winter (Fig. 6f).

Figure 9 displays the spatial distribution of the sensitivity indices of the GC, ES, and PA for the projections of the 30-yr

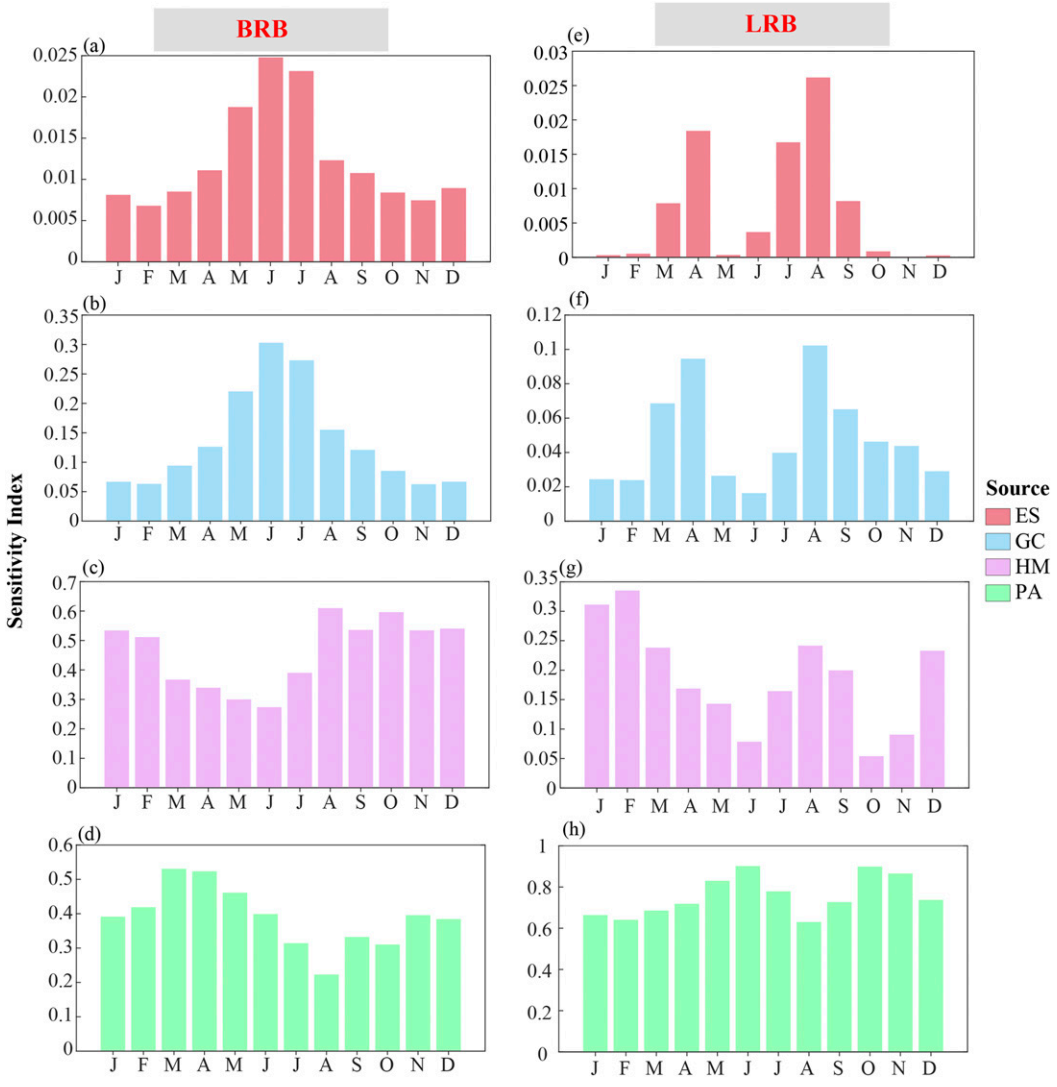

FIG. 6. Intra-annual variability of the sensitivity indices of the PA, HM, GC, and ES for the discharge projections at Hengshi station in the BRB and at Tieling station in the LRB during the future period 2071–2100. The sensitivity indices are calculated based on the four-layer HSAF [Eq. (6)].

(2071–2100) average annual surface runoff over the two basins. The main observation is that the uncertainty of the three sources is unevenly distributed over the two basins. Overall, the ranking of the uncertainty contribution is PA > GC > ES. For the BRB (Figs. 9a,b), the uncertainty of ES and GC tends to increase from upstream (no less than 0.3% and 4.1%, respectively) to downstream (no more than 2.4% and 11.8%, respectively), whereas the uncertainty of PA tends to decrease from upstream to downstream (from 95.5% to 86.3%, Fig. 9c). For the LRB, the PA and ES contribute larger uncertainties in the midstream region (no more than 0.7% and 97.7%, respectively) than in the upstream and downstream regions (no less than 0.03% and 68.4%, respectively). The opposite pattern is detected for the GC uncertainty, which makes the largest contribution (31.5%) upstream and downstream and the smallest contribution (1.7%) midstream.

Figure 10 displays the spatial distribution of the sensitivity indices of the GC, ES, and PA for the 30-yr (2071–2100) average surface runoff projections on the seasonal scale. For the BRB (Fig. 10a), the uncertainty of the ES and GC tends to increase from upstream to downstream in all seasons, while the opposite trend is identified for the PA uncertainty. The contribution of PA uncertainty is still the largest (83%–95%) and tends to be larger in autumn and winter over most of the BRB. The ES uncertainty is larger in spring and winter (especially for the downstream) and smaller in summer and autumn (especially for the upstream). The GC uncertainty is large (small) during spring and summer (autumn and winter) downstream (upstream).

For the LRB (Fig. 10b), the uncertainties of ES and GC are relatively larger in spring and winter (with averages of 2% and 15%, respectively) than in summer and autumn (with averages

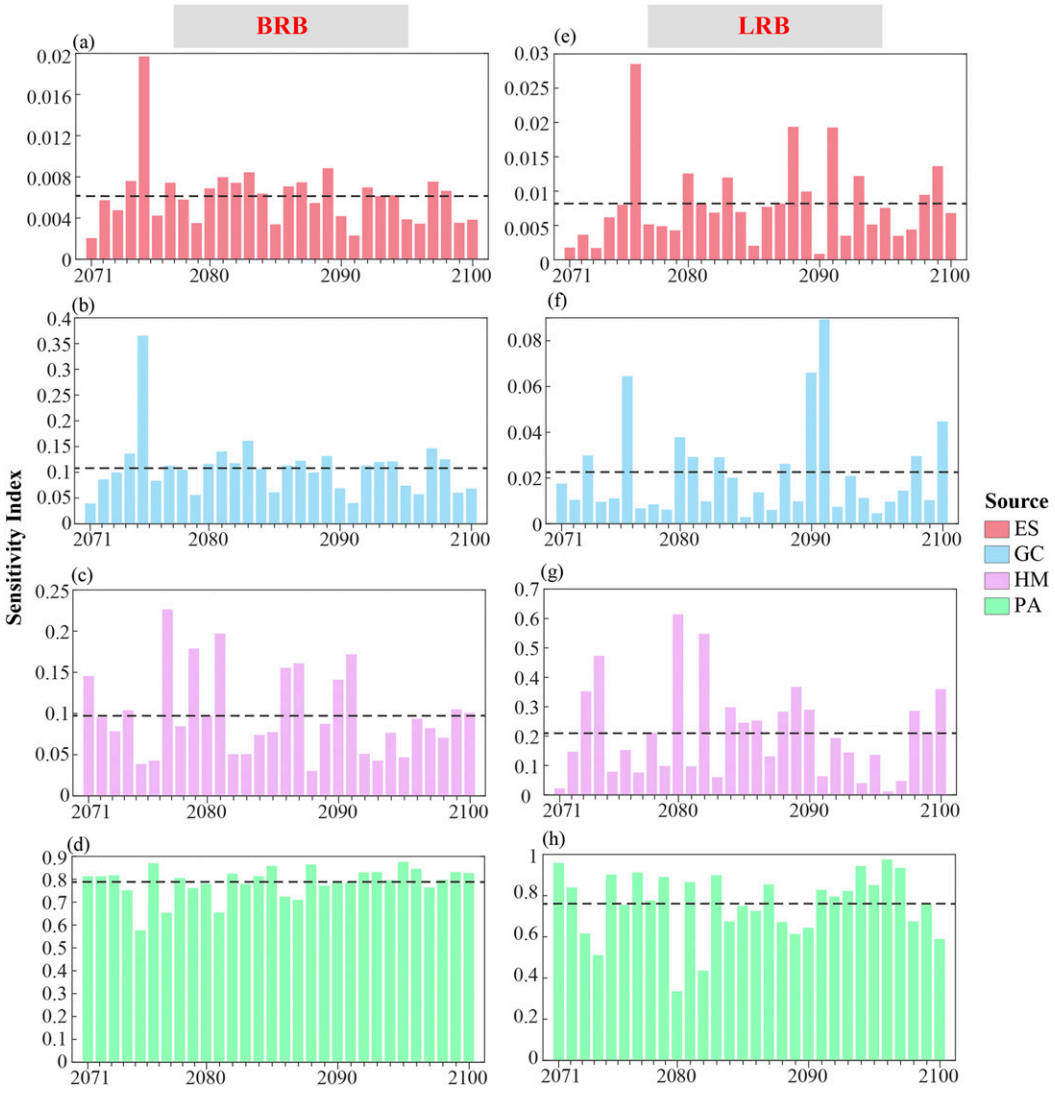

FIG. 7. Interannual variability of the sensitivity indices of the PA, HM, GC, and ES for the annual peak discharge projections at Hengshi station in the BRB and at Tieling station in the LRB during the future period 2071–2100. The sensitivity indices are calculated based on the four-layer HSAF [Eq. (6)].

of 0.5% and 2.5%, respectively). In contrast, the PA uncertainty is significantly larger in summer and autumn (with an average of 97%) and smaller in spring and winter (with an average of 85%). On the spatial scale, the GC uncertainty is significantly larger upstream for all seasons (>10%), while the PA uncertainty is generally small upstream (<90%).

5. Discussion

In this study, we extended the HSAF of Dai et al. (2017a) to quantify the relative contribution of uncertainty sources to hydrological projections under climate change on both temporal and spatial scales. The four-layer HSAF considering four uncertainty sources (i.e., ES, GC, HM, and PA) in projections of river discharge and the three-layer HSAF considering three uncertainty sources (i.e., ES, GC, and PA) in projections of surface runoff were developed and tested in both humid and semiarid basins. Different from previous studies (Dai et al. 2017a), the Morris method was used to screen the most sensitive PAs of the HMs to reduce the workload of parameter calibration and validation. Meanwhile, the LHS method was used to estimate the sensitivity indices from the sensitive PAs to reduce the computational costs. Compared with qualitative comparison methods (Chen et al. 2011b, 2013; Dobler et al. 2012) and ANOVA methods (Aryal et al. 2019; Bosshard et al. 2013; Vetter et al. 2015, 2017), the HSAF presented in this study is capable of grouping different model uncertainty sources and considering the dependence relationships among uncertainty inputs as well as the spatiotemporal variations of uncertainty sources, especially grouping the most sensitive PAs from different HMs. More importantly, this HSAF can theoretically be applied to perform quantitative analysis of

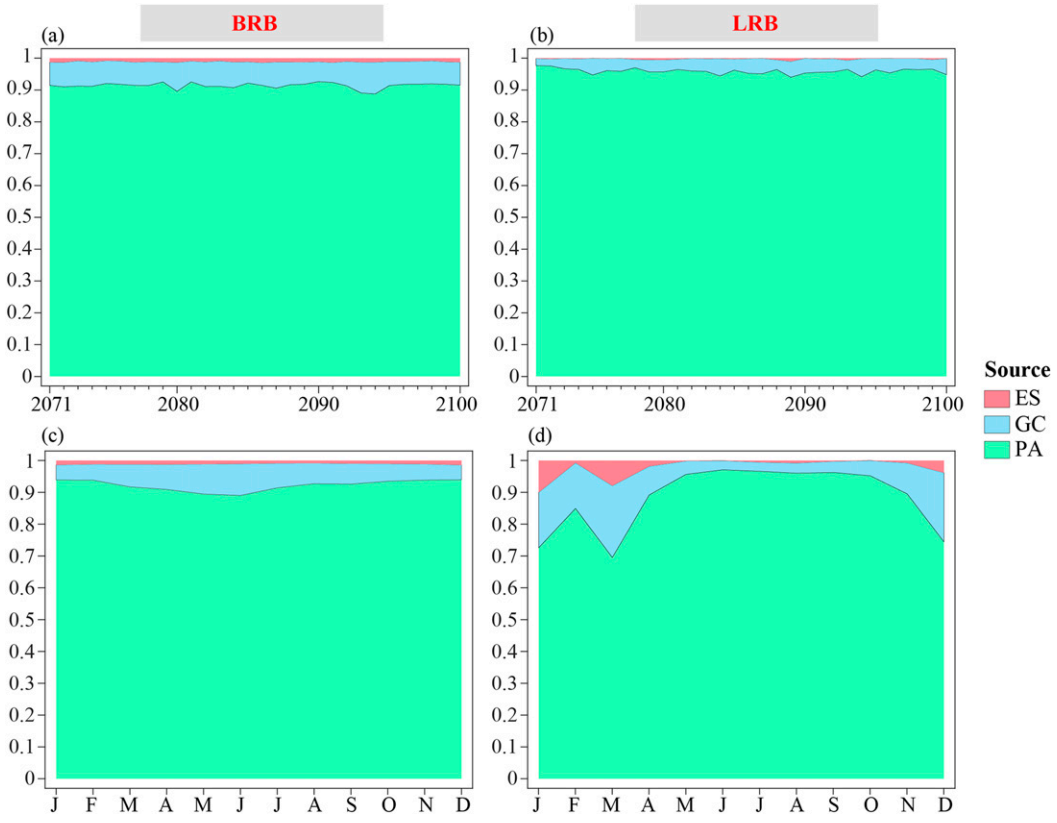

FIG. 8. Interannual variability (2071–2100) of the sensitivity indices of the PA, GC, and ES for surface runoff projections in (a) the BRB and (b) LRB. Intra-annual variability of the sensitivity indices of the PA, GC, and ES for surface runoff projections in (c) the BRB and (d) LRB. The sensitivity indices are calculated based on the three-layer HSAF [Eq. (8)].

n ($n \geq 2$) kinds of uncertain sources (e.g., GC, GC internal variability, ES, HM, PA, and downscaling methods) in the context of climate change impact studies.

The results of this study highlight the strong temporal and spatial variability of general sources of uncertainty in hydrological predictions. The ES is generally the smallest uncertainty contributor in hydrological projections, but its uncertainty shows large variability on both temporal and spatial scales (e.g., Figs. 5–7, 9, and 10), a consistent finding with the projections of extreme precipitation events (Wada et al. 2013; Xu et al. 2019) and runoff (Kay et al. 2009; Vetter et al. 2017). The HM (PA) is the largest source of uncertainty for the humid BRB (the semiarid LRB) on both interannual (Fig. 5) and intra-annual (Fig. 6) scales, a finding generally consistent with Aryal et al. (2019), which indicated that the HM contributes the largest uncertainty at dry seasons in a humid catchment of Nepal considering the GC, bias-correction methods, and HM. Compared with HM, research on the uncertainty of PA over time and space is rather lacking because most previous studies on uncertainty assessments of hydrological impacts of climate change are based on the assumption that the optimal parameter set identified in the historical period would remain valid in future projections (Aryal et al. 2019; Giuntoli et al. 2015; Su et al. 2017; Vetter et al. 2015, 2017). Using efficient sampling methods to obtain parameter samples in parameter space is one of the enhanced tools representing the uncertainty of PA.

The LHS method was applied to generate 20 sets of the most sensitive parameters for each HM to sample within a bounded sensitive parameter range, and the results highlight the large uncertainty range of PA, especially for projections of annual peak discharge (Figs. 7d,h). Particularly, the PA contributes larger uncertainty to (annual and monthly) discharge projections in the semiarid basin than the humid basin (Figs. 5d,h and 6d,h), which may be attributed to the strong responses of hydrological processes to the PAs in the semiarid basin because the adaptive range of PA is generally smaller in the semiarid basins than in humid basins (Wang et al. 2012; Xie et al. 2007). In addition, the Xinanjiang model identified more sensitive PAs for the semiarid basin (K_C, CS, and KG) than for the humid basin (SM and CS, Table 2), which may be another reason for the greater uncertainty of PA in the semiarid basin. These results also indicate that the uncertainty of PA is generally larger in projections of annual peak discharge (Fig. 7) compared with projections of annual discharge (Fig. 5), which can be mainly attributed to the larger uncertainty range of PA for annual peak discharge than for annual discharge (Figs. S3 and S5). Overall, our study suggests that the influences of PA on hydrological projections

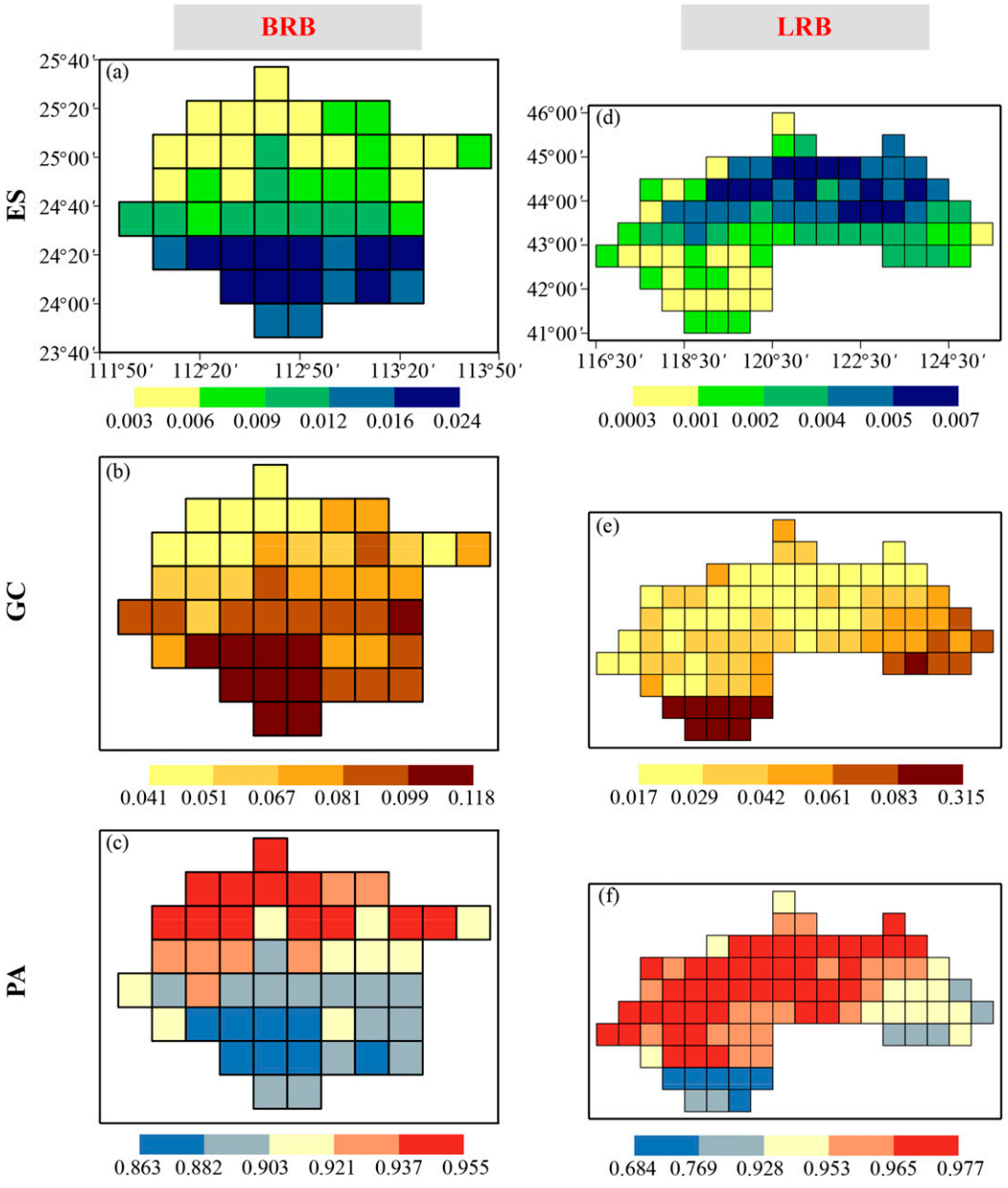

FIG. 9. Spatial distribution of the sensitivity indices of the PA, GC, and ES for the 30-yr (2071–2100) average surface runoff projections over the (left) BRB and (right) LRB. The sensitivity indices are calculated based on the three-layer HSAF [Eq. (8)].

should be considered with caution, especially for projections of extreme hydrological events.

The HM contributes greater uncertainty to the annual peak discharge projections in the semiarid basin than in the humid basin (Figs. 7c,g), probably due to the larger discrepancies in the simulations of annual peak discharge between the HMs in the semiarid basin than in the humid basin (Fig. S6). In contrast, the HM contributes greater uncertainty to annual discharge projections in the humid basin than in the semiarid basin (Figs. 5c,g and 6c,g), which can be attributed to the larger uncertainty range of annual discharge simulations of HMs in the humid basin than in the semiarid basin (Fig. S3) due to the larger discrepancies in annual discharge simulations between the VIC model and the other two HMs in the humid basin (Fig. S7).

The results also indicate that the GC contributes larger uncertainty to discharge projections in the wet season than in the dry season in the humid basin (Figs. 6b and 8c), a finding generally consistent with Aryal et al. (2019) and Hattermann et al. (2018), mainly due to the larger uncertainty range in the precipitation projections during the wet season (see Fig. S8). Most previous studies indicated that GC is one of the largest

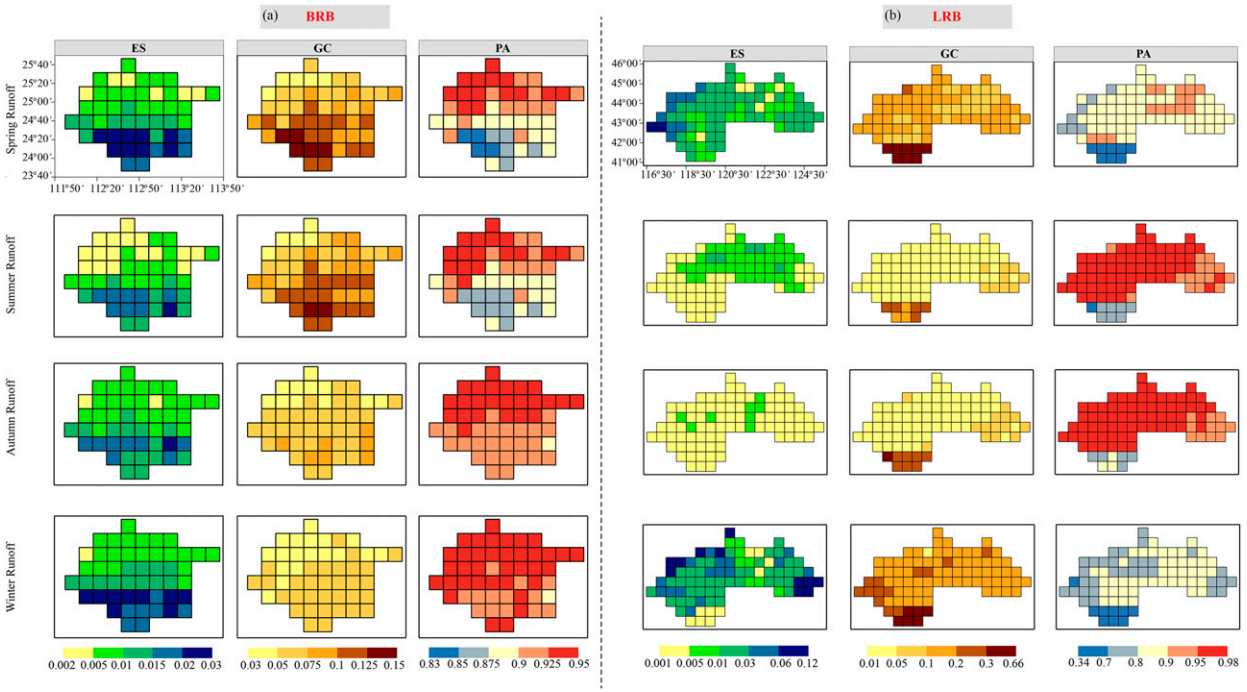

FIG. 10. Spatial distribution of the sensitivity indices of the PA, GC, and ES for the 30-yr average surface runoff projections over the (a) BRB and (b) LRB on the seasonal scale. The sensitivity indices are calculated based on the three-layer HSAF [Eq. (8)].

sources of uncertainty in climate change projections (Bosshard et al. 2013; Chen et al. 2011b; Déqué 2007; Kay et al. 2009; Prudhomme and Davies 2009; Su et al. 2017; Wilby and Harris 2006). However, our results demonstrate that the uncertainty of GC is often obscured by the PA and HM (e.g., Figs. 5b, 5f, 6b, 6f, and 8), and one of the possible reasons is that the effects of GC uncertainty are weakened after transformations using the statistical downscaling method (VB-CF). VB-CF is a simple matching of observed and modeled variables instead of the dynamic downscaling of large-scale atmospheric fields, leading to a decreased variability in GC simulations (see Fig. S1b; Wu et al. 2020).

This study is subject to a few limitations. First, only one downscaling technique was applied in this study. It is widely accepted that the uncertainty caused by the downscaling methods is potentially large (Bosshard et al. 2013). Second, we consider only two different climatic basins, which cannot represent other types of climatic zones (e.g., arid or semihumid basin) or high-latitude regions. Third, only one member of each GC was used in this study without considering the uncertainty from the internal variability of GC. Therefore, more sources of uncertainty (e.g., different downscaling techniques and multiple GC members) need to be considered within the HSAF to better understand the spatiotemporal variations of the general sources of uncertainty in hydrological predictions.

6. Conclusions

This study presents an advanced hierarchical SA of a climate-influenced hydrological model system to quantify different sources of uncertainty in the hydrological impacts of future climate change in two different climatic (humid and semiarid) basins. The HSAF is developed to be integrated with the variance-based SA method to estimate the relative importance of different uncertainty sources, including 3 ESs, 20 GCs, 3 HMs, and 20 sets of the most sensitive PAs. The Morris method was applied to screen the most sensitive parameters for different HMs, and the LHS strategy was applied to estimate the sensitivity indices for the HSAF. The spatiotemporal variability of the uncertainties in hydrological (annual discharge, annual peak discharge, and surface runoff) predictions were comparatively analyzed using the four- and three-layer HSAFs.

The parameter sensitivity results show that expM and coeM are the two most sensitive parameters of the CREST model for both basins and that SM and CS (K_C, CS, and KG) are the most sensitive parameters for the BRB (LRB). The uncertainty analysis indicates that the overall trend of uncertainty contributions to the projected discharge is PA > HM > GC > ES. However, the sources of uncertainty have significant discrepancies in the projections of different hydrological variables. The HM uncertainty in annual and monthly discharge projections tends to be larger than the PA uncertainty in the humid basin than in the semiarid basin. The PA has greater uncertainty in extreme hydrological event (annual peak discharge) projections than in annual discharge projections in both basins (particularly for the humid basin) but contributes larger uncertainty to annual and monthly discharge projections in the semiarid basin than in the humid basin. The GC contributes larger uncertainty in the projections of all the hydrological

variables in the humid basin than in the semiarid basin. Compared with other uncertainties, the ES uncertainty is rather limited in both basins. Overall, our results suggest a greater spatiotemporal variability of general sources of uncertainty in more arid regions. We also suggest that more attention should be paid to the selection of HMs for humid basins and the optimization of PAs for arid basins.

The HSAF used is mathematically rigorous and general and can be applied to a wide range of climate-influenced models with more or different sources of uncertainty. The sensitivity results can provide a better understanding of the spatiotemporal variations of various uncertainty sources in hydrological projections under climate change.

Acknowledgments. This research was supported by funding from the National Natural Science Foundation of China (Grants 51879108, 41807182, 51741903) and the Natural Science Foundation of Guangdong Province, China (Grant 2018A030310653). The daily precipitation and discharge data were provided by the Hydrology Bureau of Guangdong Province, China: http://swj.gd.gov.cn/. Daily maximum and minimum temperature data were obtained from the Meteorological Data Sharing Service System, National Meteorological Information Center, China Meteorological Administration (http://cdc.cma.gov.cn/home.do). The daily data of precipitation, maximum and minimum temperature from 20 global climate models were provided by the CMIP5 (https://esgf-node.llnl.gov/search/cmip5/).

REFERENCES

Abbaspour, K. C., M. Faramarzi, S. S. Ghasemi, and H. Yang, 2009: Assessing the impact of climate change on water resources in Iran. *Water Resour. Res.*, **45**, W10434, https://doi.org/10.1029/2008WR007615.

Alfieri, L., P. Burek, L. Feyen, and G. Forzieri, 2015: Global warming increases the frequency of river floods in Europe. *Hydrol. Earth Syst. Sci.*, **19**, 2247–2260, https://doi.org/10.5194/hess-19-2247-2015.

Arnell, N. W., 1999: Climate change and global water resources. *Global Environ. Change*, **9**, S31–S49, https://doi.org/10.1016/S0959-3780(99)00017-5.

——, 2004: Climate change and global water resources: SRES emissions and socio–economic scenarios. *Global Environ. Change*, **1**, 31–52, https://doi.org/10.1016/j.gloenvcha.2003.10.006.

Aryal, A., S. Shrestha, and M. S. Babel, 2019: Quantifying the sources of uncertainty in an ensemble of hydrological climate–impact projections. *Theor. Appl. Climatol.*, **135**, 193–209, https://doi.org/10.1007/s00704-017-2359-3.

Bastola, S., C. Murphy, and J. Sweeney, 2011: The role of hydrological modelling uncertainties in climate change impact assessments of Irish river catchments. *Adv. Water Resour.*, **34**, 562–576, https://doi.org/10.1016/j.advwatres.2011.01.008.

Bennett, K. E., J. R. Urrego Blanco, A. Jonko, T. J. Bohn, A. L. Atchley, N. M. Urban, and R. S. Middleton, 2018: Global sensitivity of simulated water balance indicators under future climate change in the Colorado Basin. *Water Resour. Res.*, **54**, 132–149, https://doi.org/10.1002/2017WR020471.

Bianchi Janetti, E., L. Guadagnini, M. Riva, and A. Guadagnini, 2019: Global sensitivity analyses of multiple conceptual models with uncertain parameters driving groundwater flow in a regional-scale sedimentary aquifer. *J. Hydrol.*, **574**, 544–556, https://doi.org/10.1016/j.jhydrol.2019.04.035.

Bosshard, T., M. Carambia, K. Goergen, S. Kotlarski, P. Krahe, M. Zappa, and C. Schär, 2013: Quantifying uncertainty sources in an ensemble of hydrological climate-impact projections. *Water Resour. Res.*, **49**, 1523–1536, https://doi.org/10.1029/2011WR011533.

Chen, J., F. P. Brissette, and R. Leconte, 2011a: Uncertainty of downscaling method in quantifying the impact of climate change on hydrology. *J. Hydrol.*, **401**, 190–202, https://doi.org/10.1016/j.jhydrol.2011.02.020.

——, ——, A. Poulin, and R. Leconte, 2011b: Overall uncertainty study of the hydrological impacts of climate change for a Canadian watershed. *Water Resour. Res.*, **47**, W12509, https://doi.org/10.1029/2011WR010602.

——, ——, D. Chaumont, and M. Braun, 2013: Performance and uncertainty evaluation of empirical downscaling methods in quantifying the climate change impacts on hydrology over two North American river basins. *J. Hydrol.*, **479**, 200–214, https://doi.org/10.1016/j.jhydrol.2012.11.062.

——, ——, P. Liu, and J. Xia, 2017: Using raw regional climate model outputs for quantifying climate change impacts on hydrology. *Hydrol. Processes*, **31**, 4398–4413, https://doi.org/10.1002/hyp.11368.

Chu-Agor, M. L., R. Muñoz-Carpena, G. Kiker, A. Emanuelsson, and I. Linkov, 2011: Exploring vulnerability of coastal habitats to sea level rise through global sensitivity and uncertainty analysis. *Environ. Modell. Software*, **26**, 593–604, https://doi.org/10.1016/j.envsoft.2010.12.003.

Dai, H., and M. Ye, 2015: Variance-based global sensitivity analysis for multiple scenarios and models with implementation using sparse grid collocation. *J. Hydrol.*, **528**, 286–300, https://doi.org/10.1016/j.jhydrol.2015.06.034.

——, X. Chen, M. Ye, X. Song, and J. M. Zachara, 2017a: A geostatistics-informed hierarchical sensitivity analysis method for complex groundwater flow and transport modeling. *Water Resour. Res.*, **53**, 4327–4343, https://doi.org/10.1002/2016WR019756.

——, M. Ye, A. P. Walker, and X. Chen, 2017b: A new process sensitivity index to identify important system processes under process model and parametric uncertainty. *Water Resour. Res.*, **53**, 3476–3490, https://doi.org/10.1002/2016WR019715.

——, X. Chen, M. Ye, X. Song, G. Hammond, B. Hu, and J. M. Zachara, 2019: Using Bayesian networks for sensitivity analysis of complex biogeochemical models. *Water Resour. Res.*, **55**, 3541–3555, https://doi.org/10.1029/2018WR023589.

Demaria, E. M., B. Nijssen, and T. Wagener, 2007: Monte Carlo sensitivity analysis of land surface parameters using the Variable Infiltration Capacity model. *J. Geophys. Res.*, **112**, D11113, https://doi.org/10.1029/2006JD007534.

Déqué, M., 2007: Frequency of precipitation and temperature extremes over France in an anthropogenic scenario: Model results and statistical correction according to observed values. *Global Planet. Change*, **57**, 16–26, https://doi.org/10.1016/j.gloplacha.2006.11.030.

Dick, J., F. Y. Kuo, and I. H. Sloan, 2013: High-dimensional integration: The quasi-Monte Carlo way. *Acta Numer.*, **22**, 133–288, https://doi.org/10.1017/S0962492913000044.

Dobler, C., S. Hagemann, R. L. Wilby, and J. Stotter, 2012: Quantifying different sources of uncertainty in hydrological projections in an Alpine watershed. *Hydrol. Earth Syst. Sci.*, **16**, 4343–4360, https://doi.org/10.5194/hess-16-4343-2012.

Gädeke, A., H. Hölzel, H. Koch, I. Pohle, and U. Grünewald, 2014: Analysis of uncertainties in the hydrological response of a

model-based climate change impact assessment in a sub-catchment of the Spree River, Germany. *Hydrol. Processes*, **28**, 3978–3998, https://doi.org/10.1002/hyp.9933.

Giuntoli, I., J.-P. Vidal, C. Prudhomme, and D. M. Hannah, 2015: Future hydrological extremes: The uncertainty from multiple global climate and global hydrological models. *Earth Syst. Dyn.*, **6**, 267–285, https://doi.org/10.5194/esd-6-267-2015.

Gou, J., C. Miao, Q. Duan, Q. Tang, Z. Di, W. Liao, J. Wu, and J. Wu, 2020: Sensitivity analysis-based automatic parameter calibration of the VIC model for streamflow simulations over China. *Water Resour. Res.*, **56**, e2019WR025968, https://doi.org/10.1029/2019WR025968.

Guth, P. A., V. Kaarnioja, F. Y. Kuo, C. Schillings, and I. H. Sloan 2019: A quasi-Monte Carlo method for an optimal control problem under uncertainty. ArXiv, 34 pp., https://arxiv.org/abs/1910.10022.

Habets, F., and Coauthors, 2013: Impact of climate change on the hydrogeology of two basins in northern France. *Climatic Change*, **121**, 771–785, https://doi.org/10.1007/s10584-013-0934-x.

Hansen, M. C., R. S. Defries, J. R. G. Townshend, and R. Sohlberg, 2000: Global land cover classification at 1 km spatial resolution using a classification tree approach. *Int. J. Remote Sens.*, **21**, 1331–1364, https://doi.org/10.1080/014311600210209.

Hattermann, F. F., and Coauthors, 2018: Sources of uncertainty in hydrological climate impact assessment: A cross-scale study. *Environ. Res. Lett.*, **13**, 015006, https://doi.org/10.1088/1748-9326/aa9938.

Hawkins, E., T. M. Osborne, C. K. Ho, and A. J. Challinor, 2013: Calibration and bias correction of climate projections for crop modelling: An idealised case study over Europe. *Agric. For. Meteor.*, **170**, 19–31, https://doi.org/10.1016/j.agrformet.2012.04.007.

He, J., K. Yang, W. Tang, H. Lu, J. Qin, Y. Chen, and X. Li, 2020: The first high-resolution meteorological forcing dataset for land process studies over China. *Sci. Data*, **7**, 25, https://doi.org/10.1038/s41597-020-0369-y.

Helton, J. C., and F. J. Davis, 2003: Latin hypercube sampling and the propagation of uncertainty in analyses of complex systems. *Reliab. Eng. Syst. Saf.*, **81**, 23–69, https://doi.org/10.1016/S0951-8320(03)00058-9.

Hoegh-Guldberg, O., and J. F. Bruno, 2010: The impact of climate change on the world's marine ecosystems. *Science*, **328**, 1523–1528, https://doi.org/10.1126/science.1189930.

Iman, R. L., and W. J. Conover, 1980: Small sample sensitivity analysis techniques for computer models with an application to risk assessment. *Commun. Stat. Theory Methods*, **9**, 1749–1842, https://doi.org/10.1080/03610928008827996.

IPCC, 2007: *Climate Change 2007: The Physical Science Basis.* Cambridge University Press, 996 pp.

——, 2013: *Climate Change 2013: The Physical Science Basis.* Cambridge University Press, 1535 pp., https://doi.org/10.1017/CBO9781107415324.

Jha, M. K., and P. W. Gassman, 2014: Changes in hydrology and streamflow as predicted by a modelling experiment forced with climate models. *Hydrol. Processes*, **28**, 2772–2781, https://doi.org/10.1002/hyp.9836.

Jiang, T., Y. Q. Chen, C. Y. Xu, X. H. Chen, X. Chen, and V. P. Singh, 2007: Comparison of hydrological impacts of climate change simulated by six hydrological models in the Dongjiang Basin, South China. *J. Hydrol.*, **336**, 316–333, https://doi.org/10.1016/j.jhydrol.2007.01.010.

Jung, M., and Coauthors, 2010: Recent decline in the global land evapotranspiration trend due to limited moisture supply. *Nature*, **467**, 951–954, https://doi.org/10.1038/nature09396.

Kay, A. L., H. N. Davies, V. A. Bell, and R. G. Jones, 2009: Comparison of uncertainty sources for climate change impacts: Flood frequency in England. *Climatic Change*, **92**, 41–63, https://doi.org/10.1007/s10584-008-9471-4.

Khorashadi Zadeh, F., J. Nossent, F. Sarrazin, F. Pianosi, A. van Griensven, T. Wagener, and W. Bauwens, 2017: Comparison of variance-based and moment-independent global sensitivity analysis approaches by application to the SWAT model. *Environ. Modell. Software*, **91**, 210–222, https://doi.org/10.1016/j.envsoft.2017.02.001.

Liang, X., D. P. Lettenmaier, E. F. Wood, and S. J. Burges, 1994: A simple hydrologically based model of land surface water and energy fluxes for general circulation models. *J. Geophys. Res.*, **99**, 14 415–14 428, https://doi.org/10.1029/94JD00483.

Lin, K., F. Lv, L. Chen, V. P. Singh, Q. Zhang, and X. Chen, 2014: Xinanjiang model combined with Curve Number to simulate the effect of land use change on environmental flow. *J. Hydrol.*, **519**, 3142–3152, https://doi.org/10.1016/j.jhydrol.2014.10.049.

Liu, J., X. Chen, J. Zhang, and M. Flury, 2009: Coupling the Xinanjiang model to a kinematic flow model based on digital drainage networks for flood forecasting. *Hydrol. Processes*, **23**, 1337–1348, https://doi.org/10.1002/hyp.7255.

Liu, L., T. Fischer, T. Jiang, and Y. Luo, 2013: Comparison of uncertainties in projected flood frequency of the Zhujiang River, South China. *Quat. Int.*, **304**, 51–61, https://doi.org/10.1016/j.quaint.2013.02.039.

Lohmann, D., E. Raschke, B. Nijssen, and D. P. Lettenmaier, 1998: Regional scale hydrology: I. Formulation of the VIC-2L model coupled to a routing model. *Hydrol. Sci. J.*, **43**, 131–141, https://doi.org/10.1080/02626669809492107.

Lu, W., W. Wang, Q. Shao, Z. Yu, Z. Hao, W. Xing, B. Yong, and J. Li, 2018: Hydrological projections of future climate change over the source region of Yellow River and Yangtze River in the Tibetan Plateau: A comprehensive assessment by coupling RegCM4 and VIC model. *Hydrol. Processes*, **32**, 2096–2117, https://doi.org/10.1002/hyp.13145.

Matthews, J. H., and T. L. Quesne, 2009: Adapting Water Management: A Primer on Coping with Climate Change. WWF Water Security Series 3, 36 pp., http://assets.wwf.org.uk/downloads/water_management.pdf.

Maurer, E. P., and P. B. Duffy, 2005: Uncertainty in projections of streamflow changes due to climate change in California. *Geophys. Res. Lett.*, **32**, L03704, https://doi.org/10.1029/2004GL021462.

McKay, M. D., R. J. Beckman, and W. J. Conover, 1979: A comparison of three methods for selecting values of input variables in the analysis of output from a computer code. *Technometrics*, **21**, 239–245, https://doi.org/10.2307/1268522.

Minville, M., F. Brissette, and R. Leconte, 2008: Uncertainty of the impact of climate change on the hydrology of a Nordic watershed. *J. Hydrol.*, **358**, 70–83, https://doi.org/10.1016/j.jhydrol.2008.05.033.

Morris, M. D., 1991: Factorial sampling plans for preliminary computational experiments. *Technometrics*, **33**, 161–174, https://doi.org/10.1080/00401706.1991.10484804.

Najafi, M. R., H. Moradkhani, and I. W. Jung, 2011: Assessing the uncertainties of hydrologic model selection in climate change impact studies. *Hydrol. Processes*, **25**, 2814–2826, https://doi.org/10.1002/hyp.8043.

Neuman, S. P., 2003: Maximum likelihood Bayesian averaging of uncertain model predictions. *Stochastic Environ. Res. Risk Assess.*, **17**, 291–305, https://doi.org/10.1007/s00477-003-0151-7.

Nijssen, B., D. P. Lettenmaier, X. Liang, S. W. Wetzel, and E. F. Wood, 1997: Streamflow simulation for continental-scale river basins. *Water Resour. Res.*, **33**, 711–724, https://doi.org/10.1029/96WR03517.

Nóbrega, M. T., W. Collischonn, C. E. M. Tucci, and A. R. Paz, 2011: Uncertainty in climate change impacts on water resources in the Rio Grande Basin, Brazil. *Hydrol. Earth Syst. Sci.*, **15**, 585–595, https://doi.org/10.5194/hess-15-585-2011.

Piao, S., and Coauthors, 2010: The impacts of climate change on water resources and agriculture in China. *Nature*, **467**, 43–51, https://doi.org/10.1038/nature09364.

Preston, B. L., 2002: Aquatic ecosystems and global climate change. *Limnol. Oceanogr. Bull.*, **11**, 22–22, https://doi.org/10.1002/lob.200211122.

Prudhomme, C., and H. Davies, 2009: Assessing uncertainties in climate change impact analyses on the river flow regimes in the UK. Part 2: Future climate. *Climatic Change*, **93**, 197–222, https://doi.org/10.1007/s10584-008-9461-6.

Raje, D., and P. P. Mujumdar, 2010: Hydrologic drought prediction under climate change: Uncertainty modeling with Dempster–Shafer and Bayesian approaches. *Adv. Water Resour.*, **33**, 1176–1186, https://doi.org/10.1016/j.advwatres.2010.08.001.

Refsgaard, J. C., J. P. van der Sluijs, A. L. Højberg, and P. A. Vanrolleghem, 2007: Uncertainty in the environmental modelling process – A framework and guidance. *Environ. Modell. Software*, **22**, 1543–1556, https://doi.org/10.1016/j.envsoft.2007.02.004.

Ren, Q. W., Y. B. Chen, and X. J. Shu, 2010: Global sensitivity analysis of Xinanjiang model parameters based on Extend FAST method (in Chinese). *Acta Sci. Nat. Univ. Sunyatseni*, **49**, 127–134.

Rubin, Y., X. Chen, H. Murakami, and M. Hahn, 2010: A Bayesian approach for inverse modeling, data assimilation, and conditional simulation of spatial random fields. *Water Resour. Res.*, **46**, W10523, https://doi.org/10.1029/2009WR008799.

Saltelli, A., 2000: What is sensitivity analysis? *Sensitivity Analysis*, A. Saltelli, K. Chan, and M. Scott, Eds., Wiley, 3–14.

——, and I. M. Sobol', 1995: Sensitivity analysis for nonlinear mathematical models: Numerical experience. *Inst. Math. Modell.*, **7**, 16–28.

——, S. Tarantola, and K. Chad, 1998: Presenting results from model based studies to decision makers: Can sensitivity analysis be a defogging agent? *Risk Anal.*, **18**, 799–803, https://doi.org/10.1111/j.1539-6924.1998.tb01122.x.

——, ——, and P. S. Chan, 1999: A quantitative model independent method for global sensitivity analysis of model output. *Technometrics*, **41**, 39–56, https://doi.org/10.1080/00401706.1999.10485594.

——, P. Annoni, I. Azzini, F. Campolongo, M. Ratto, and S. Tarantola, 2010: Variance based sensitivity analysis of model output. Design and estimator for the total sensitivity index. *Comput. Phys. Commun.*, **181**, 259–270, https://doi.org/10.1016/j.cpc.2009.09.018.

Shen, M., J. Chen, M. Zhuan, H. Chen, C. Y. Xu, and L. Xiong, 2018: Estimating uncertainty and its temporal variation related to global climate models in quantifying climate change impacts on hydrology. *J. Hydrol.*, **556**, 10–24, https://doi.org/10.1016/j.jhydrol.2017.11.004.

Sobol', I. M., 1993: Sensitivity analysis for nonlinear mathematical models. *Math. Model. Comput. Exp.*, **1**, 407–414.

Song, X., F. Kong, C. Zhan, J. Han, and X. Zhang, 2013: Parameter identification and global sensitivity analysis of Xin'anjiang model using meta-modeling approach. *Water Sci. Eng.*, **6**, 1–17, https://doi.org/10.3882/j.issn.1674-2370.2013.01.001.

——, J. Zhang, C. Zhan, Y. Xuan, M. Ye, and C. Xu, 2015: Global sensitivity analysis in hydrological modeling: Review of concepts, methods, theoretical framework, and applications. *J. Hydrol.*, **523**, 739–757, https://doi.org/10.1016/j.jhydrol.2015.02.013.

Stephens, C. M., F. M. Johnson, and L. A. Marshall, 2018: Implications of future climate change for event–based hydrologic models. *Adv. Water Resour.*, **119**, 95–110, https://doi.org/10.1016/j.advwatres.2018.07.004.

Su, B., J. Huang, X. Zeng, C. Gao, and T. Jiang, 2017: Impacts of climate change on streamflow in the upper Yangtze River basin. *Climatic Change*, **141**, 533–546, https://doi.org/10.1007/s10584-016-1852-5.

Tang, G., Z. Zeng, D. Long, X. Guo, B. Yong, W. Zhang, and Y. Hong, 2016: Statistical and hydrological comparisons between TRMM and GPM level-3 products over a midlatitude basin: Is Day-1 IMERG a good successor for TMPA 3B42V7? *J. Hydrometeor.*, **17**, 121–137, https://doi.org/10.1175/JHM-D-15-0059.1.

Tartakovsky, D. M., 2013: Assessment and management of risk in subsurface hydrology: A review and perspective. *Adv. Water Resour.*, **51**, 247–260, https://doi.org/10.1016/j.advwatres.2012.04.007.

Teng, J., J. Vaze, F. H. Chiew, B. Wang, and J. Perraud, 2012: Estimating the relative uncertainties sourced from GCMs and hydrological models in modeling climate change impact on runoff. *J. Hydrometeor.*, **13**, 122–139, https://doi.org/10.1175/JHM-D-11-058.1.

Teutschbein, C., F. Wetterhall, and J. Seibert, 2011: Evaluation of different downscaling techniques for hydrological climate–change impact studies at the catchment scale. *Climate Dyn.*, **37**, 2087–2105, https://doi.org/10.1007/s00382-010-0979-8.

Thompson, J. R., A. J. Green, D. G. Kingston, and S. N. Gosling, 2013: Assessment of uncertainty in river flow projections for the Mekong River using multiple GCMs and hydrological models. *J. Hydrol.*, **486**, 1–30, https://doi.org/10.1016/j.jhydrol.2013.01.029.

Valkó, É., T. Varga, A. S. Tomlin, Á. Busai, and T. Turányi, 2018: Investigation of the effect of correlated uncertain rate parameters via the calculation of global and local sensitivity indices. *J. Math. Chem.*, **56**, 864–889, https://doi.org/10.1007/s10910-017-0836-7.

van Griensven, A., T. Meixner, S. Grunwald, T. Bishop, M. Diluzio, and R. Srinivasan, 2006: A global sensitivity analysis tool for the parameters of multi-variable catchment models. *J. Hydrol.*, **324**, 10–23, https://doi.org/10.1016/j.jhydrol.2005.09.008.

van Vuuren, D. P. V., and Coauthors, 2011: The representative concentration pathways: An overview. *Climatic Change*, **109**, 5–31, https://doi.org/10.1007/s10584-011-0148-z.

Vetter, T., S. Huang, V. Aich, T. Yang, X. Wang, V. Krysanova, and F. Hattermann, 2015: Multi-model climate impact assessment and intercomparison for three large-scale river basins on three continents. *Earth Syst. Dyn.*, **6**, 17–43, https://doi.org/10.5194/esd-6-17-2015.

——, and Coauthors, 2017: Evaluation of sources of uncertainty in projected hydrological changes under climate change in 12 large-scale river basins. *Climatic Change*, **141**, 419–433, https://doi.org/10.1007/s10584-016-1794-y.

Vörösmarty, C. J., P. Green, J. Salisbury, and R. B. Lammers, 2000: Global water resources: Vulnerability from climate change

and population growth. *Science*, **289**, 284–288, https://doi.org/10.1126/science.289.5477.284.

Wada, Y., and Coauthors, 2013: Multimodel projections and uncertainties of irrigation water demand under climate change. *Geophys. Res. Lett.*, **40**, 4626–4632, https://doi.org/10.1002/grl.50686.

Wang, G. Q., and Coauthors, 2012: Assessing water resources in China using PRECIS projections and a VIC model. *Hydrol. Earth Syst. Sci.*, **16**, 231–240, https://doi.org/10.5194/hess-16-231-2012.

Wang, J., and Coauthors, 2011: The coupled routing and excess storage (CREST) distributed hydrological model. *Hydrol. Sci. J.*, **56**, 84–98, https://doi.org/10.1080/02626667.2010.543087.

Wang, L., R. Ranasinghe, S. Maskey, P. H. A. J. M. van Gelder, and J. K. Vrijling, 2016: Comparison of empirical statistical methods for downscaling daily climate projections from CMIP5 GCMs: A case study of the Huai River Basin, China. *Int. J. Climatol.*, **36**, 145–164, https://doi.org/10.1002/joc.4334.

Wang, P. L., and R. J. Zhao, 1989: Examination of parameters of Xinanjiang model (3 components) (in Chinese). *J. Hohai Univ.*, **17**, 16–21.

Wilby, R. L., 2005: Uncertainty in water resource model parameters used for climate change impact assessment. *Hydrol. Processes*, **19**, 3201–3219, https://doi.org/10.1002/hyp.5819.

——, and I. Harris, 2006: A framework for assessing uncertainties in climate change impacts: Low-flow scenarios for the River Thames, UK. *Water Resour. Res.*, **42**, W02419, https://doi.org/10.1029/2005WR004065.

Wu, C., G. Huang, H. Yu, Z. Chen, and J. Ma, 2014: Impact of climate change on reservoir flood control in the upstream area of the Beijiang River basin, South China. *J. Hydrometeor.*, **15**, 2203–2218, https://doi.org/10.1175/JHM-D-13-0181.1.

Wu, C. H., G. R. Huang, and H. J. Yu, 2015: Prediction of extreme floods based on CMIP5 climate models: A case study in the Beijiang River basin, South China. *Hydrol. Earth Syst. Sci.*, **19**, 1385–1399, https://doi.org/10.5194/hess-19-1385-2015.

——, P. J.-F. Yeh, Y. Y. Chen, B. X. Hu, and G. R. Huang, 2020: Future precipitation-driven meteorological drought changes in the CMIP5 multimodel ensembles under 1.5°C and 2°C global warming. *J. Hydrometeor.*, **21**, 2177–2196, https://doi.org/10.1175/JHM-D-19-0299.1.

Xie, Z., F. Yuan, Q. Duan, J. Zheng, M. Liang, and F. Chen, 2007: Regional Parameter estimation of the VIC land surface model: Methodology and application to river basins in China. *J. Hydrometeor.*, **8**, 447–468, https://doi.org/10.1175/JHM568.1.

Xu, K., B. Xu, J. Ju, C. Wu, H. Dai, and B. X. Hu, 2019: Projection and uncertainty of precipitation extremes in the CMIP5 multimodel ensembles over nine major basins in China. *Atmos. Res.*, **226**, 122–137, https://doi.org/10.1016/j.atmosres.2019.04.018.

Xu, Y. P., X. Zhang, Q. Ran, and Y. Tian, 2013: Impact of climate change on hydrology of upper reaches of Qiantang River Basin, East China. *J. Hydrol.*, **483**, 51–60, https://doi.org/10.1016/j.jhydrol.2013.01.004.

Xue, X., Y. Hong, A. S. Limaye, J. J. Gourley, G. J. Huffman, S. I. Khan, C. Dorji, and S. Chen, 2013: Statistical and hydrological evaluation of TRMM-based Multi-satellite Precipitation Analysis over the Wangchu Basin of Bhutan: Are the latest satellite precipitation products 3B42V7 ready for use in ungauged basins? *J. Hydrol.*, **499**, 91–99, https://doi.org/10.1016/j.jhydrol.2013.06.042.

Yang, J., 2011: Convergence and uncertainty analyses in Monte-Carlo based sensitivity analysis. *Environ. Modell. Software*, **26**, 444–457, https://doi.org/10.1016/j.envsoft.2010.10.007.

Yao, C., K. Zhang, Z. Yu, Z. Li, and Q. Li, 2014: Improving the flood prediction capability of the Xinanjiang model in ungauged nested catchments by coupling it with the geomorphologic instantaneous unit hydrograph. *J. Hydrol.*, **517**, 1035–1048, https://doi.org/10.1016/j.jhydrol.2014.06.037.

Zeng, X., D. Wang, and J. Wu, 2012: Sensitivity analysis of the probability distribution of groundwater level series based on information entropy. *Stochastic Environ. Res. Risk Assess.*, **26**, 345–356, https://doi.org/10.1007/s00477-012-0556-2.

Zhang, H., G. H. Huang, D. Wang, and X. Zhang, 2011: Uncertainty assessment of climate change impacts on the hydrology of small prairie wetlands. *J. Hydrol.*, **396**, 94–103, https://doi.org/10.1016/j.jhydrol.2010.10.037.

Zhao, R., Y. Zhuang, L. Fang, X. Liu, and Q. Zhang, 1980: The Xinanjiang model. *IAHS Publ.*, **129**, 351–356.

Zhao, R. J., 1992: The Xinanjiang model applied in China. *J. Hydrol.*, **135**, 371–381, https://doi.org/10.1016/0022-1694(92)90096-E.

——, and X. R. Liu, 1995: The Xinanjiang model. *Computer Models of Watershed Hydrology*, V. Singh, Ed., Water Resources Publications, 215–232.